

## ARTICLE OPEN



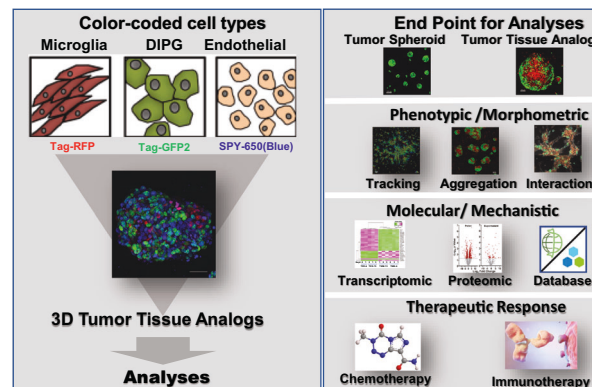
# Multicellular tumor-stromal interactions recapitulate aspects of therapeutic response and human oncogenic signaling in a 3D disease model for H3K27M-altered DIPG

© The Author(s) 2025

It has become evident from decades of clinical trials that multimodal therapeutic approaches with focus on cell intrinsic and microenvironmental cues are needed to improve understanding and treat the rare, inoperable, and ultimately fatal diffuse intrinsic pontine glioma (DIPG), now categorized as a diffuse midline glioma. In this study we report the development and characterization of an in vitro system utilizing 3D Tumor Tissue Analogs (TTA), designed to replicate the intricate DIPG microenvironment. The innate ability of fluorescently labeled human brain endothelial cells, microglia, and patient-derived DIPG cell lines to self-assemble has been exploited to generate multicellular 3D TTAs that mimic tissue-like microstructures, enabling an in-depth exploration of the spatio-temporal dynamics between neoplastic and stromal cells. The 3D-TTA model recapitulates clinical patterns of DIPG growth, evidenced by resistance to chemotherapy, HDAC and proteasome inhibitors, as well as sensitization to the antibody-activated innate immune microenvironment including complement proteins and surrounding microglia. Multimodal fluorescence imaging platforms integrated with high-throughput omics revealed that alterations in tumor cell motility and growth in the 3D-TTA model compared to tumor cell only spheroids correlated with specific transcriptomic and proteomic changes. STAT3, ITGA5, LGALS1, SOD2, MVP, and CLIC1, associated with microenvironment signaling, DNA replication, and immune regulation, were identified as potential novel targets in the 3D model. The results indicate that the 3D TTA platform developed here represents a powerful tool for preclinical studies, paving the way for identification/validation of tissue specific biomarkers and novel drug targets, thus advancing disease management strategies for DIPG in children.

*Oncogene* (2025) 44:3694–3712; <https://doi.org/10.1038/s41388-025-03533-7>

## Graphical Abstract



## HIGHLIGHTS

1. Bottom-up Reductionist Approach: Optimization of a tumor permissive stromal Niche for DIPG.
2. Stromalized 3D clusters impact the growth and co-migration of tumor cells.
3. Tumor-stromal cell interaction modifies the molecular signature of tumor cells.
4. Clinical relevance of DIPG tumor tissue analogs.

A full list of authors and their affiliations appears at the end of the paper.

Received: 10 December 2024 Revised: 15 July 2025 Accepted: 4 August 2025

Published online: 6 September 2025

## INTRODUCTION

Reclassified in 2016 (WHO) as a grade IV malignant midline glioma (DMG), diffuse intrinsic pontine glioma (DIPG), is a highly aggressive tumor of the brain stem that is difficult to treat and is a leading cause of brain cancer deaths among children [1]. With 150–300 new diagnoses per year in the United States, DIPG has a devastating impact on children and families, with a median survival ranging from 8 to 12 months and a projected 5-year survival of ~2% [2]. The diffuse invasive phenotype of DIPG, together with the proximity to vital brainstem structures, renders resection impossible [3, 4]. Treatment modalities such as fractionated radiation therapy (RT), the established standard-of-care, offer limited benefits [5], prolonging survival by ~3 months on average [6]. Thus, outcomes have not changed substantially over the past decades [7–9], in part because of therapeutic resistance and the risks associated with invasive procedures for acquisition of biopsy tissues to study the molecular characteristics of the disease [10]. Benefitting from the contemporary improved understanding of the tumor ecosystem, implementation of immunotherapy, as a promising treatment option, is ongoing [11, 12].

Epigenetic modulation resulting from single amino acid substitution of lysine (K) 27 to methionine (M) in histone H3 (H3K27M) within the brainstem is a currently well-understood driver of tumorigenesis in most DIPG/DMG cases [13, 14]. The neurogenic niche comprised of signaling factors, extracellular matrix (ECM) and specialized cell types such as microvascular endothelial cells and microglia contribute to a distinctive microenvironment that may support self-renewal or “stemness” in H3K27M variants as well as resistance to therapy [15]. Characterization of the dynamic reciprocity in the tumor microenvironment (TME) that promotes therapeutic resistance is ongoing and of high clinical relevance. Nevertheless, the prognosis remains dismal, even after >250 clinical trials performed over the past three decades [16, 17]. This suggests that using in vitro models that better account for microenvironmental cues affecting tumor-intrinsic and immunogenic targets may provide better insights [7, 18, 19]. Therefore, identifying the critical tumor-cell interactions in the DIPG microenvironment is an essential step towards improved understanding of the disease process that impacts pharmacologic development and clinical outcome [20].

Preclinical results at times fail to translate into benefits for humans in clinical trials, a relatively common occurrence in DIPG. Immune compromised human xenograft or orthotopic models for DIPG use rodents that are often 6–8 weeks of age (corresponding to 20–30 human years), which is potentially problematic for translation to an illness that typically arises in children aged 5–9 yrs [16]. Genetically engineered immune competent mouse models (GEMM) for DIPG generate brainstem tumors de novo sharing molecular signatures of pathology found in the human disease [21–23]. They are valuable in determining the specific genetic alterations driving tumor formation and growth. The antitumor activity of therapeutic agents as observed in these animal models remains to be demonstrated in children with DIPG. Preclinical in vitro studies in DIPG that preceded validation in animal models have included neurospheres or adherent monolayers from patient-derived cell cultures [24–27]. The culture conditions in these models can lead to significant differences in gene expression and signaling pathways that influence the response of DIPG cells to potential therapies [28]. A comprehensive approach including multiple experimental models leveraging the strengths of each in representing the malignancy while allowing for controlled experimental manipulation in a reproducible and cost-effective manner are needed for optimal drug testing and translation of findings to patients. Our effort here is to introduce a simple and practical 3D co-culture model that complements the existing preclinical model systems to assist in

the identification of stroma-induced molecular targets and a more reliable projection of the therapeutic response in children.

The present work is grounded on the hypothesis that the invasive nature and hard-to-treat phenotype of DIPG may be associated with dynamic crosstalk between tumor cells and the microenvironment [29, 30]. These midline brainstem tumors harbor an immunologically cold TME with myeloid cells including microglia and tumor-associated macrophages as the most abundant immune cell population amidst proliferating vascular endothelial cells and pericytes [29–31]. From a critical introspection analysis of the available literature for representative in-vitro DIPG/DMG models, envisaged as rapid, reproducible and cost-effective screening platforms with potential for therapeutic validation and discovery, a reductionist methodology offered the most logical bottom-up approach. More importantly, the 3D platform has been conceived to recreate the evolving TME by sequential introduction of other DIPG tissue specific components.

We present here a model for the *H3K27M-altered* DIPG TME that includes tumor tissue analogs (TTA) formed through 3D co-culture, with monitored size, cell number, and cellular composition. These TTAs are capable of self-assembling into tissue-like microstructures. The miniaturized 3D disease model for DIPG allows controlled manipulation of the microenvironment and therapeutic intervention in real-time as monitored by standardized imaging. Exploiting the 3D TTA to elucidate the mechanistic basis of microenvironment-induced changes in tumor cells by integrating proteomic and transcriptomic analysis provides insights into chemotherapy resistance and the molecular basis of stroma-induced synthetic lethality of immunotherapeutic approaches in DIPG. Such progress made toward an improved therapeutic strategy for DIPG can lead to neuro-oncologic advances of high importance and may provide therapeutic targets for validation in clinical trials.

## MATERIALS AND METHODS

### Cell lines

All cell lines were maintained at 37°C and 5% CO<sub>2</sub> as 2D or 3D cultures. Patient-derived non-adherent DIPG cell lines, SU-DIPG-6 (H3.3-K27M, female), SU-DIPG-13 (H3.3-K27M, female), SU-DIPG-17 (H3.3-K27M, male), SU-DIPG-4 (H3.1-K27M, female), were gifted by Dr. Michelle Monje's laboratory at Stanford University [32]. Cells were cultured in Tumor Stem Media (TSM) consisting of a 1:1 mixture of DMEM/F12 (Invitrogen, Carlsbad, CA, USA) and Neurobasal (-A) medium (Invitrogen) with 0.1 mg/ml Primocin (InvivoGen, #ant-pm-1, San Diego, CA, USA), and supplemented with B27(-A) (Invitrogen), human-βFGF (20 ng/mL), human-EGF (20 ng/mL), human PDGF-AA (20 ng/mL), human PDGF-BB (20 ng/mL) all from Shenandoah Biotechnology, Warminster, PA, USA and heparin (10 ng/mL) (StemCell Technologies, Vancouver, Canada). Patient-derived SF8628 cell line (H3.3-K27M, female) was purchased from EMD Millipore (SCC127) and maintained in DMEM-High Glucose (Sigma, D6546, St. Louis, MO, USA), 10% Fetal Bovine Serum (FBS, ATCC® 30202™, Manassas, VA, USA), 2 mM L-Glutamine (EMD Millipore Cat. No. TMS-002-C, Darmstadt, Germany) and 0.1 mg/ml Primocin.

Other pediatric brain tumor cell lines (Neuroblastoma, Medulloblastoma and Glioblastoma) were used to assess relative expression of the tumor specific antigen, GD2 in DIPG cells and were provided by the Asgharzadeh laboratory (CHLA). Patient-derived MYCN non-amplified human neuroblastoma cell lines CHLA-15 (female) and L-AN-6 (male) were established in the Seeger laboratory (CHLA) [33]. CHLA-15 cells were grown in IMDM (Gibco Cat. No. 12440053, Grand Island, New York, USA) with 20% FBS, 4mM L-glutamine, and 1X ITS (5 µg/mL insulin, 5 µg/mL transferrin, 5 ng/mL selenous acid, Cat. No. 41-400-045, Gibco). L-AN-6 cells were grown in RPMI-1640 plus 10% FBS, and 2mM L-glutamine. MYCN-driven 9464D neuroblastoma cell line derived from transgenic mice [34] was cultured in DMEM supplemented with 10% FBS, 1 mM sodium pyruvate, 2 µM L-glutamine, 1X MEM nonessential amino acids, and 0.1 mg/ml Primocin. D54 (adult glioblastoma; female) and UW-228-2 (SHH-activated pediatric medulloblastoma; female) cell lines were maintained in DMEM with 10% FBS and 0.1 mg/ml Primocin. SV40-immortalized human microglial cells HMC-3 (ATCC®CRL-3304) were cultured in EMEM (ATCC® 30-2003™)

supplemented with 10% FBS and 0.1 mg/ml Primocin. SV40-immortalized human cerebral microvascular endothelial cells, HBEC-5i (ATCC® CRL-3245), were grown in DMEM:F12 (ATCC® 30-2006™) with 10% FBS and 40 µg/ml endothelial cell growth supplement (ECGS, EMD Millipore #02-102). All cell lines were authenticated by short tandem repeat DNA profiling (University of Arizona Genetic Core, Tucson, AZ) performed every two years, and tested for mycoplasma contamination three days before an experiment (Mycoalert Detection kit, Lonza, LT07-705, Rockville, MD, USA).

#### Transient labeling of endothelial cells for detecting dynamic tumor-stromal cell interactions

SPY650-DNA (Spirochrome AG, SC-501, Stein am Rhein, Switzerland) is a far-red ( $\lambda_{\text{abs/em}}$  652/654 nm), nontoxic, cell-permeable, and highly specific live cell DNA probe for fluorescence imaging of nucleus and DNA. A 1000x SPY650-DNA stock solution was reconstituted in 50 µL of anhydrous DMSO. Staining at this concentration allowed persistence of the dye in long term cultures, despite necessary media change and ongoing cell division. HBEC-5i microvascular endothelial cells at a 60–70% confluency were incubated overnight with staining solution of SPY650-DNA in a 1:3000 dilution of fresh cell culture medium as described. The single-cell suspension of labeled endothelial cells was then used for multicellular 3D co-cultures.

#### Generation of lentivirus-transduced stable fluorescent cell lines

Lentivirus-based labeling reagents enabling co-expression of a nuclear-restricted green (tagGFP2) or orange (tagRFP) fluorescent protein, as well as puromycin driven by an EF-1 $\alpha$  promoter were purchased from Sartorius (Cat. No. 4624 & 4771, Göttingen, Germany). Polyclonal DIPG cell lines expressing tagGFP2 (GFP), and HMC3 microglial cell line expressing tagRFP (RFP) were generated in-house as per the manufacturer's instructions. Briefly, cells were seeded at 30% confluency and were transduced 18–24 h later with lentivirus particles at an MOI (multiplicity of infection) of 3 using standard fresh medium supplemented with Polybrene® (Millipore Sigma, TR-1003-G, Burlington, MA, USA) at concentration of 8 µg/mL. The cultures were replaced with fresh medium and microscopically evaluated for expression of fluorescent proteins 48–72 h later. Fluorescent cells were enriched by puromycin (Gibco, A11138-03) selection (0.5 µg/mL) after 48–72 h, later followed by flow sorting. Each fluorescent cell line was checked for mycoplasma contamination and identity by STR analysis.

#### Establishment of 3D tumor tissue analogs for DIPG

We describe a technique for self-assembly of monodispersed cells to generate tumor tissue analogs (TTA) of multiple cell types that can be precisely size-controlled and can influence the DIPG microenvironment. Multicellular 3D aggregates were cultured from a combination of (i) SU-DIPG-6 and SU-DIPG-13 cell lines, stably transduced to express nuclear restricted green (tagGFP2) fluorescent protein, (ii) human brain microglial cells (HMC-3), transduced to express red (tagRFP) fluorescent protein, and (iii) untransduced human cerebral microvascular endothelial cells (HBEC-5i), visualized as needed via staining with a fluorescent dye (SPY650) as described below. The 3D multicellular tissue-like aggregates are formed and maintained in the same serum-free medium supplemented with brain specific growth factors [35]. Clear flat or round bottom, low attachment 96-well plates (Corning, NY) were used in experimental studies with 15,000 to 45,000 cells/well for 96-well flat- and U-bottom plates or 60,000 cells/well for 8-well micro chamber slides (ibidi, Gräfelfing, Germany). Cell counts and viability were determined using Countess 3 automated Cell Counter (Invitrogen) before plating. The 3D TTA were imaged using a STELLARIS 5 confocal microscope (Leica Microsystems, Deerfield, IL, USA). Confocal z-stacks were acquired, maximum intensity projections were generated, and spatial measurements were performed using Leica LAS X software. Violin plots were generated with GraphPad Prism.

#### Phase-contrast time-lapse microscopy

Time-lapse fluorescence and phase-contrast microscopy were performed using a Zeiss Axio Observer 7 live cell imaging microscope (Carl Zeiss Microimaging, Thornwood, NY, USA) with 5x or 10x objectives and a custom-stage incubator to house 3D culture samples in an 8-well micro chamber slide (ibidi, 80826 Fitchburg, WI, USA). Quantitative data were obtained from an average of 108 images per experimental condition at each timepoint (Nine fields of view were examined per condition, performed separately in four dishes, and with each experiment repeated a total of three times). Images were acquired every 30 min over a course of

48 h and each image sequence contained approximately 108 frames of 0.65 µm/pixel.

#### Tracking tumor cell migration

Images acquired with time lapse microscopy were analyzed using the Imaris 9.9.1 (Bitplane AG, Zurich, Switzerland) software with spot detection function to track migration of nuclear restricted GFP-expressing SU-DIPG cells alone and in co-culture with stromal cells. Spot size was set to 10 µm as an upper threshold for background signal filtration. Autoregressive motion was used for tracking and “maxDistance” was designated as 30 µm with a “Maximum Gap Size” of 3 frames between each track. The integrated “Edit Tracks” function in the Imaris software was used to correct for potentially fragmented and/or falsely connected tracks. The integrated “statistics” function was additionally used to extract data for track length, average speed, average displacement, and straightness of tumor cell trajectories. Cell tracks were graphically represented using MATLAB (Portola Valley, CA, USA).

#### Immunohistochemistry (IHC)

IHC was performed on Formalin-fixed Paraffin-embedded 3D Tumor cell only cultures (T) and Tumor Tissue Analogs (TEM) using the automated Leica BOND RX platform. Briefly, the slides were heated at 60°C for 10 min and deparaffinized using Dewax (Leica Biosystems, Buffalo Grove, IL, USA) at 72°C for 30 s; Sequentially rinsed with three changes of 100% reagent alcohol followed by rinse in Bond Wash (3 min), and DI water (4 min). Antigen retrieval was done with ER1 buffer at 100°C for 20 min. Samples were then incubated in hydrogen peroxide for 10 min, and rinsed three times with Bond Wash (2 min each) again and incubated for 1 h with either of the following primary antibodies from Abcam: (a) Olig2 (1:125, ab109186), CD133 (1:1000, ab216323), GFAP (1:2000, ab7260), Ki-67 (1:800, ab15580), CD31 (1:100, ab9498), or IBA-1 (1:100, PA527436, Fisher Scientific); rinsed three times in Bond Wash, for 2 min each. The BOND Refine (DS9800; Leica Biosystems) detection system was used for visualization. Slides were then dehydrated, cleared, and coverslipped. Images were viewed using Aperio ImageScope software (Version v12.4.6.5003, Leica Biosystems, Milton Keynes, UK).

#### Histone extraction and Histone H3 Methylated trimethyl Lys27 ELISA

Histones were extracted by standard extraction techniques using the Active Motif Histone Extraction Minikit (40026). Histone ELISAs were conducted using the trimethyl K27 Elisa Kit (Active Motif, 53106) normalized to a H3K27me3 standard curve and total H3 protein. 4 µg of total histone protein was used per antibody binding reaction in the ELISA. The experiment was repeated 3 times with three replicates per sample. The absorbance was read at 450 nm and 655 nm that served as the reference wavelength for background subtraction. The absorbance values of the unknown samples were then used to interpolate their protein concentrations from the standard curve generated on graphpad prism.

#### Mass spectrometry-based proteomics of 3D cell cultures

DIPG cells only in 3D cultures and DIPG cells in co-culture with endothelial cells and microglia were collected at day 5, 10 and 15 for proteomic analysis. The cultures were maintained for 5 days in the same medium, after which the medium in each sample was replaced every 2 days. Total protein from each sample (supernatant and 3D cell cultures) was reduced, alkylated, and purified by chloroform/methanol extraction prior to digestion with sequencing grade modified porcine trypsin (Promega, Madison, WI, USA). Tryptic peptides were then separated by reverse phase XSelect CSH C18 2.5 µm resin (Waters, Milford, MA, USA) on an in-line 150 × 0.075 mm column using an UltiMate 3000 RSLCnano system (Thermo Fisher Scientific, Waltham, MA USA). Peptides were eluted using a 90 min gradient from 98:2 to 65:35 buffer A:B ratio (Buffer A = 0.1% formic acid, 0.5% acetonitrile; Buffer B = 0.1% formic acid, 99.9% acetonitrile). Eluted peptides were ionized by electrospray (2.4 kV) followed by mass spectrometric analysis on an Orbitrap Eclipse Tribrid mass spectrometer (Thermo Fisher Scientific). Mass spectrometry (MS) data were acquired using a Fourier transform mass spectrometry analyzer in profile mode of full width at half maximum (FWHM) resolution of 120,000 over a range of 375 to 1400 m/z with advanced peak determination. Following HCD (high energy collisional dissociation) activation, tandem mass spectrometry (MS/MS) data were acquired using the ion trap analyzer in centroid mode and normal mass range with a normalized collision energy of 30%.



Proteins were identified by query of the Uniprot Homo Sapiens Database (June 2021) using MaxQuant (version 2.0.3.0, Max Planck Institute, Martinsried, Germany) with a parent ion tolerance of 3 ppm and a fragment ion tolerance of 0.5 Da. Scaffold Q + S (Proteome Software, Portland, OR, USA) was used to verify MS/MS based peptide and protein identifications. Protein identifications were accepted if they could be recognized with less than 1.0% false discovery and contained at least 2 identified peptides. Protein probabilities were assigned by the edge features. Protein MS1 iBAQ intensity values were assessed for quality using ProteiNorm [36]. The data were normalized using variance stabilizing normalization (VSN) and statistical analysis was performed using Linear Models for Microarray Data (limma) with empirical Bayes (eBayes) smoothing of the standard errors [37]. Proteins with an FDR adjusted *p*-value < 0.05 and a fold change > 2 were considered significant.

### Flow cytometry to detect surface expression of GD2 on tumor cell lines

Cells were detached using trypsin (0.05%) with EDTA, washed in complete media and pelleted by centrifugation. They were counted and  $5 \times 10^5$  cells were washed once in cold FACS buffer (1X PBS supplemented with 2% heat-inactivated FBS and 2 mM EDTA and the endocytosis inhibitor NaN<sub>3</sub>) followed by incubation with anti-GD2-APC antibody (Clone 14G2a, Isotype mouse IgG2a, BD Biosciences, Franklin Lakes, NJ, USA) or isotype-matched control mAb of irrelevant specificity (murine IgG2a-APC; BD Biosciences) for 30 min in a 4 °C ice water bath in the dark. Cells were washed twice in FACS buffer and transferred to filter top tubes with addition of DAPI live/dead stain (final concentration 1 µg/ml; Sigma-Aldrich). Data were acquired using a BD FACS Aria I flow cytometer, acquiring 10,000 events from the live (DAPI negative) singlet gate for each cell line. Exported Flow Cytometry Standard (fcs) files were then analyzed using FlowJo\_v10 software (Ashland, OR, USA) and geometric mean fluorescence intensity determined for every sample. The stain index, which is the mean fluorescence intensity (MFI) of the positive and negative populations divided by two times the standard deviation (SD) of the negative population was calculated for each cell line and graphically represented. Stain Index ( $\Delta$ ) = MFI (positive) – MFI (negative) / 2 X SD (negative)

### Whole blood collection and plasma preparation

Human whole blood was collected from four IRB-consented healthy donors (CHLA-21-00319) by venipuncture in EDTA-sprayed lavender top BD Vacutainer® collection tubes. Samples were obtained after informed consent, and in accordance with an institutional review board approved protocol. Cells were separated from plasma by centrifugation for 15 min at 1500 x g using a refrigerated centrifuge. The resulting supernatant, designated as plasma, was aliquoted and stored at –80 °C.

### Imaging and analysis in real time by IncuCyte

Live cell imaging was performed using IncuCyte S3 (Sartorius). SU-DIPG-6 and/or SU-DIPG-13 cells were seeded alone and in co-culture with stromal cells and scanned on 96-well flat bottom

(CytoOne, CC7682-7596, USA Scientific, Ocala, FL, USA) or U-bottom (Corning, 7007, Corning, NY, USA) plates in the cell culture incubator over time. Each well was scanned using a 10X objective lens in 4 randomly selected positions or with a 4X objective at a single position, repeated at indicated intervals in the experiment. Imaging included high-definition phase contrast and epifluorescence microscopy with 483/506 and 555/584 nm filter sets to detect green (tagGFP2, DIPG) and orange (tagRFP, microglia) fluorescence, respectively. Image processing and cell counting were performed using IncuCyte software (Sartorius). There were 3 to 6 replicates for each sample set per experiment ( $r=3-6$ ) and each experiment was repeated 3 times ( $n=3$ ).

### Immunotherapeutic targeting of GD2 expressing DIPG cells in 3D co-cultures

Suspension of nuclear restricted GFP-expressing SU-DIPG-6 cells at a cell density of 15,000/well and 45,000/well and suspension of SU-DIPG-6 cells in equal proportion with stromal endothelial cells and nuclear restricted tagRFP-expressing microglial cells at a cell density of 45,000 cells/well were plated in a 96-well flat bottom plate (CytoOne, US Scientific) overnight. Cell counts and viability were determined using Countess 3 automated Cell Counter (Invitrogen) before plating. Targeting of GD2-expressing DIPG cells alone and in co-culture was assessed with IncuCyte S3 live-image fluorescent microscopy system (Sartorius) housed in a cell

culture incubator. Cytotoxicity assays were performed utilizing dinutuximab (Unituxin™, United Therapeutics Oncology, Silver Spring, MD, USA) and Plasma collected from human donors. Dinutuximab stocks and human plasma from different donors were diluted in TSM medium with growth factors before addition to wells. Final concentrations in a final well volume of 200 µl were in the following range: dinutuximab (0.5 µg/ml); Human Plasma (10%). Cultures with and without dinutuximab and Heat inactivated human plasma served as control. Cell survival for all groups was normalized to cell survival in cultures that were untreated.

### Samples preparation and RNA sequencing

GFP-expressing SU-DIPG-6 and SU-DIPG-13 cells were flow sorted from 3D cultures of tumor cells only and TTA comprised of tumor cells with microglia and endothelial cells on day 5. The SMART-Seq V4 Ultra Low RNA Input Kit for Sequencing (Takara Bio, Kusatsu, Shiga, Japan) was used for reverse transcription and generation of double stranded cDNA for subsequent library preparation using the Nextera XT Library Preparation kit (Illumina, San Diego, CA, USA). An input of 10 ng RNA was used for oligo(dT)-primed reverse transcription, followed by cDNA amplification and cleanup. Quantification of cDNA was performed using Qubit™ 4 fluorometer (Thermo Fisher Scientific). cDNA normalized to 80 pg/µl was fragmented and sequencing primers added simultaneously. A limiting-cycle PCR added Index 1 (i7) adapters, Index 2 (i5) adapters, and sequences required for cluster formation on the sequencing flow cell. Indexed libraries were pooled. Enriched libraries were verified using 2100 Bioanalyzer (Agilent Technologies, Santa Clara, CA, USA) and quantified via Qubit™ 4 fluorometer (Thermo Fisher Scientific). Libraries were sequenced on a NovaSeq 6000 (Illumina) using 1x75 bp read length and coverage of over 30 M reads/sample. Raw sequence data was deposited to NCBI GEO (GSE222891).

### Data analysis

Sequences were aligned to Ensembl genes version 107 corresponding to the Genome Research Consortium Homo sapiens build number 38 (GRCh38.p13) using the STAR aligner with 'GeneCounts' output [38]. Reads per kilobase of the transcript, per million mapped reads (RPKM) values were determined with the R/Bioconductor software package 'edgeR' [39, 40] and differential gene expression was determined using the software, 'limma-voom' [41]. Principle component plots and dendrograms of hierarchical clustering were generated from RPKM using the R software 'ggdendro' [42]. Volcano plots and heatmaps were generated using RPKM values and the R software 'gplots' [43] of differentially expressed genes. Gene set enrichment analysis was performed on differentially expressed genes with fold change >1.5 or <-1.5 using the Gene Ontology resource: 'GOSTats' [44], and target gene/protein networks were constructed using open source String database [45] and Cytoscape [46] softwares. Connectivity map (CMap) analysis was performed for high scoring genes (<https://clue.io>) to search for potential small molecule compounds. Genes found to be highly significant in the unsupervised analysis were input into The Broad Institute CMap ([clue.io](https://clue.io)) for gene set testing against the latest version of the L1000 dataset (CMap LINC5 2020) containing over 3 million gene expression profiles. The output is a list of "perturbagens" (chemicals, and biologics) that closely match the input (+ raw\_cs) and the inverse of the input (- raw\_cs).

Parametric t-test at significance level ( $\alpha=0.05$ ) was used to assess significant differential change on log-transformed values of the tracking parameters including mean speed, track length, displacement, and straightness between tumor-cell only culture (T) and co-culture (TEM) conditions with the R Statistical Package (Version 4.3.2). Box-whisker plots of the log-transformed values representing the median, 25% percentile, and 75% percentile were presented for visualization of the differential change.

## RESULTS

### 3D TTA: An in vitro robust and reproducible 3D platform integrating DIPG microenvironment

Inspired by the reductionist approach, we devised an in vitro disease model for DIPG via self-assembly of select non-malignant stromal with malignant cell types of human origin including microvascular brain endothelial cells, microglia, and tumor cell lines to form 3D tumor tissue analogs. The nomenclature followed across all sections in the manuscript for the tumor-cell-only culture



is **T** and the co-culture leading to the formation of 3D TTA comprised of tumor cells, endothelial cells and microglia is **TEM**. Lentivirus-mediated stable overexpression of nuclear restricted GFP (green fluorescence protein, tagGFP2) in H3K27M mutant-DIPG cells and of RFP (orange/red fluorescence protein, tagRFP) in microglia. The lentiviral transduction was found to impair the ability of endothelial cells to proliferate. Therefore, a live cell permeable fluorescent nuclear DNA dye, spirochrome 650 (SPY-650) was used to stain endothelial cells (blue) to distinguish them from other stably transduced cell types in the 3D TTA (Fig. 1A). The expression of IBA1 and GFAP in the microglia and CD31 in the endothelial cells in the formalin-fixed Paraffin-embedded (FFPE) sections of 3D TTA (TEM-13 and TEM-6) assessed via immunohistochemical analysis confirmed their presence in the co-cultures (Fig. 1B and Supplementary Fig. 1A). The actively proliferating tumor cells in the 3D TTA organized towards the periphery at day 5 of co-culture. These cells were strongly positive for Ki67 staining. The tumor cells in TEM-13 stained positive for expression of Olig2 (oligodendrocyte transcription factor), GFAP (glial fibrillary acid protein), and CD133, markers used to assess the differentiation and malignancy of the DMG/DIPG phenotype (Fig. 1C). These tumor specific proteins were also expressed in the FFPE sections of tumor cell only cultures (T-13) [Supplementary Fig. 1B]. Significant loss of trimethylation in Histone 3 Lysine 27 residue ( $p < 0.05$ ) of the SU-DIPG-13 cells (T-13) alone and those enriched by flow sorting (T-13 TEM sorted) from 3D TTA in comparison to TEM-13 co-culture and endothelial cells (grey asterisk) or microglia (red asterisk) was revealed upon performing an enzyme linked immunosorbent assay (ELISA) with 4  $\mu\text{g}$  of total core histones per sample (Fig. 1D). The histone 3 trimethylation in DIPG cells from tumor cell only cultures versus tumor cells sorted by flow cytometry was also found to be higher. The finding reveals that co-culturing DIPG cells with stromal cell types in a 3D environment preserves the TME characteristics of the DIPG tissue, which is a significant step towards developing more realistic in vitro models capable of complementing the preclinical in vivo investigation to advance DIPG research.

### Spatial and temporal dynamics between tumor and stromal cells impact the formation of 3D TTA

Time-lapse microscopy tracking every 30 min for 28 h was used to capture GFP-expressing DIPG cell movement, which was analyzed with the Imaris software. Transient or stable expression of fluorescent proteins in the multicellular co-cultures showed that DIPG, microglia, and endothelial cells stained with SPY-650 engage in direct contact, extend cellular processes, and migrate in spatial patterns during the formation of 3D TTA (Fig. 2 & videos in Supplementary Fig. 2). This behavior was found to be qualitatively dissimilar from the growth and aggregation of DIPG cells cultured alone, which migrated to a limited degree and did not extend cellular processes. Tracking parameters were monitored for each DIPG cell in the tumor-cell-only (T) culture and TEM co-culture conditions included speed, length, displacement, and straightness (total displacement  $\div$  track length). Figure 3A provides representative images of track speed mean, which is one of the multiple spatiotemporal measures described in Supplementary Fig. 3. The live tumor cell tracking videos from which the images and data were collected can be found in Supplementary Fig. 4. These data indicate that the presence of microglia and endothelial cells affect the movement of DIPG cells and formation of 3D microstructures. Quantitative analysis using two DIPG cell lines for speed mean is presented in the corresponding box-whisker plots of log10 transformed values shown in Fig. 3B. Parametric t-test at significance level ( $\alpha = 0.05$ ) rejected the null hypothesis of no differential change between tumor-cell only culture (T-6, T-13) and co-culture (TEM6, TEM13). Parametric t-tests resulted in a  $p$ -value  $< 2.2\text{e-}16$  for mean speed, track length, displacement and straightness when comparing T-6

and TEM-6 were significant. Similarly, for the comparison of T-13 and TEM-13, analysis resulted in  $p$ -value  $< 1.4\text{e-}05$  for track length,  $p$ -value  $< 2\text{e-}16$  for mean speed,  $p$ -value  $< 3.4\text{e-}15$  for straightness and  $p$ -value  $< 2.2\text{e-}16$  for displacement. These data provide evidence that stromal cell types promote tumor cell motility and indicate that interaction of DIPG cells with cell types of the supporting tissue environment may facilitate the transition from confined to diffusive movement.

We utilized SU-DIPG-6 cells and a high throughput system (Sartorius IncuCyte® S3) to discern morphometric characteristics during formation of 3D aggregates. Results of cluster count, cluster area, and tumor cell count were evaluated with 3 replicates within each of the 3 repeated experiments and compared between tumor cell only culture and TTA from co-culture (Fig. 3C, D). The experimental design included GFP-expressing DIPG cells that were plated alone at different densities corresponding to the tumor (T) cell count and the total cell count in the co-culture (TEM) to isolate the impact of stromal cells from the effect of cell-cell contact or confluency on the formation of aggregates and tumor cell proliferation via the IncuCyte. This live cell analysis system provided us with a reliable method for monitoring tumor cell growth in real time, allowing us to quantify the number of GFP-expressing tumor cells. The increase in tumor cell count is correlated with their proliferation over time. For the co-culture, the number of 2000  $\mu\text{m}^2$  or larger aggregates (cluster count) peaked at 6 h, then plateaued before a decreasing trend after 24 h. This reduction in the number of aggregates was also accompanied by a gradual increase in the percentage of area covered by cells (% cluster area confluence) at 24 h, indicating the growth and coalescence of smaller aggregates with multicellular composition into larger aggregates. Aggregation was less pronounced in tumor cell-only cultures, including those plated at the same confluency (45 K cells) or at one-third confluency (15 K cells) matching the DIPG cell count in the co-culture. An increase in the number of the GFP-expressing SU-DIPG cells in 3D co-cultures was observed at  $\sim 2$  days, with continued increase over the entire observation period of 5 days, (Fig. 3D, right). In contrast, the count of GFP-expressing DIPG cells in tumor cell-only culture decreased with time when plated at high confluency, with a gradual increase at one-third confluency, further indicating the impact of resource limitations on DIPG cell proliferation in tumor cell only cultures. These results suggest that stromal cell types modulate DIPG cell motility and proliferation in addition to the spontaneous tendency to aggregate into heterotypic clusters.

### Stromal cell types augment the spheroid-forming potential of 3D TTA and the proliferation of DIPG cells

Using confocal fluorescence microscopy to characterize the self-assembly process during the co-cultures, we observed spontaneous aggregation of DIPG and stromal cells into significantly larger circular microtissue-like structures that were designated 3D TTA. Aggregation occurred within 3-5 days of co-culture in flat or U-bottom 96-well plates. Fig. 4A (A, B, E, & F) provides representative bright field and confocal images of 3D clusters of non-adherent GFP-expressing H3K27M mutated SU-DIPG-6 and SU-DIPG-13 cells alone (T-6 & T-13) and in co-culture with RFP-expressing microglia (M) and non-fluorescent endothelial cells (E) (TEM-6 & TEM-13) on flat or U-bottom 96-well plates. Empirical evaluation of the spheroid/cluster size at day 5 (Fig. 4A: C, D, G & H) showed that the co-culture of stromal cell types with the DIPG cells (TEM-6 & TEM-13; 16–25 replicates per sample set) consistently yielded robust 3D TTA that were notably larger than clusters of tumor cells alone (T-6 & T-13). Multiple aggregates of variable sizes were formed in DIPG-only cultures ( $0.07\text{--}0.7 \times 10^5 \mu\text{m}^2$ ) in both flat- and U-bottom plates within 3-5 days of culture, while growth of the TEM TTA model resulted in a single large 3D TTA  $\sim 4\text{--}6 \times 10^5 \mu\text{m}^2$  in size in each well of the U-bottom plates over the same timeframe. The flat-, or U-bottom nature of

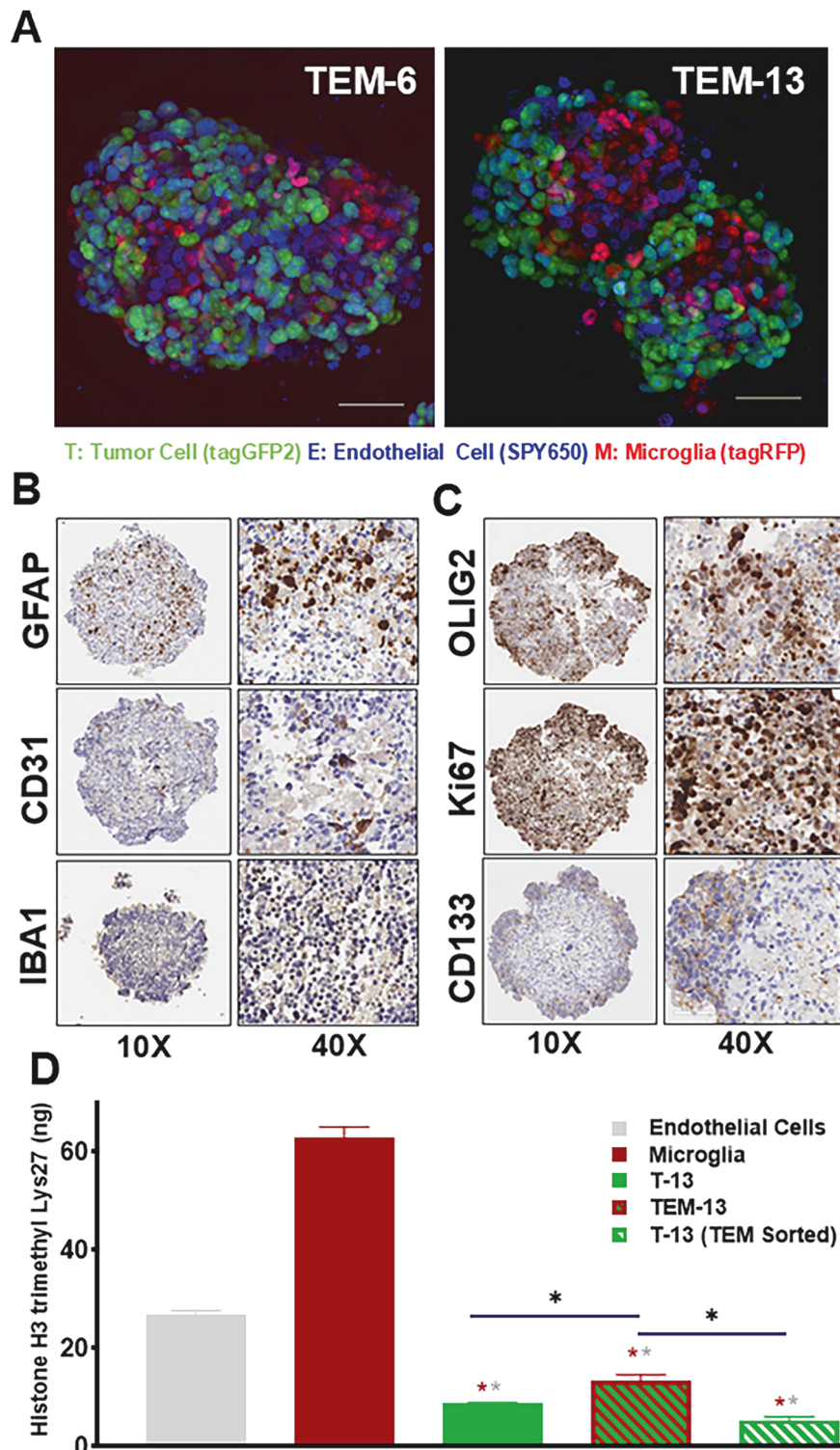


**Fig. 1 Non-adherent DIPG cells self-organize with stromal cell types into multicellular tumor tissue analogs in different 3D co-culture platforms.** **A** Presence of the three cell types in 3D TTA of TEM-6 and TEM-13 at day 5 of suspension culture is demonstrated in representative confocal merge of images with DIPG cells (T, nuclear restricted tagGFP2, green), microglia (M, nuclear restricted tagRFP; red/pink) and endothelial cells (E, SPY650 live cell fluorescent nuclear DNA dye, blue). All cells have SPY-650 stain, but it is salient in endothelial cells, which lack fluorescent proteins. Representative bright field and fluorescence images of cultures on day 5 in 96-well flat-bottom. Immunohistochemical staining (DAB) for **B** GFAP, CD31 and IBA1 identifies the presence of DIPG cells, endothelial cells and microglia and **C** CD133, Olig2 and Ki67, markers representative of DIPG /tumor stem cells in FFPE sections of the 3D TTA (TEM-6 and TEM-13); **D**, Graphical representation of Histone 3 trimethylation at Lysine 27 residue (ng) observed by ELISA performed with 4  $\mu$ g total histone protein isolated from the indicated samples. Loss of trimethylation in Histone 3 Lysine 27 residue ( $p < 0.05$ ) of the SU-DIPG-13 cells (T-13) alone and those enriched by flow sorting (T-13 TEM Sorted) from 3D TTA was significant in comparison to TEM-13 co-culture and endothelial cells (grey asterisk) or microglia (red asterisk).



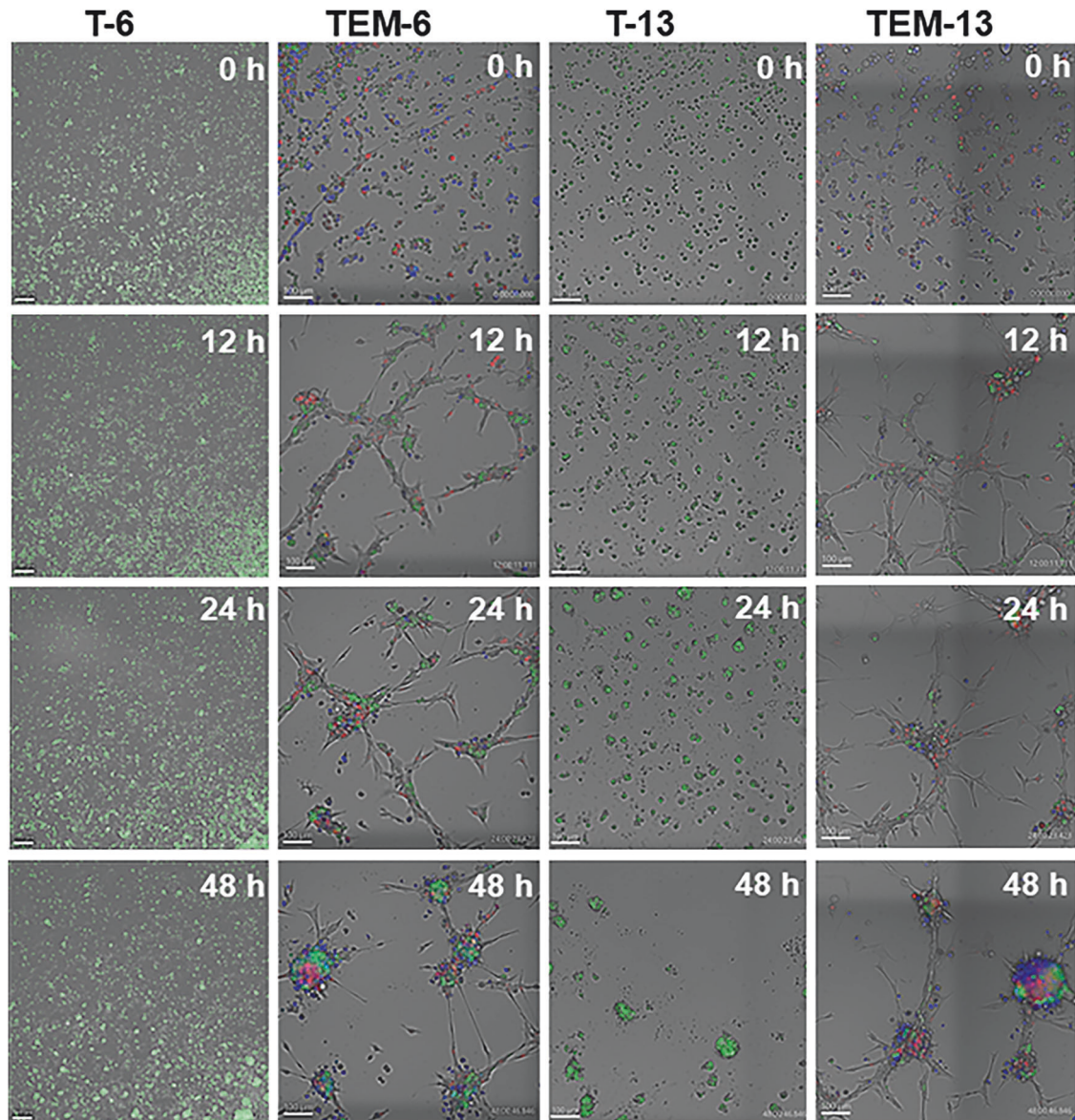


**Fig. 2 Spatio-temporal interaction between DIPG and stromal cell types Impacts formation of Tumor Tissue Analogs.** Snapshots from widefield time lapse microscopy (Zeiss Axio Observer 7) at 0, 12, 24, and 48 h of tumor, endothelial, and microglial cell co-cultures (TEM) and tumor cells cultured alone; –6 and –13 refer to cultures of SU-DIPG-6 and SU-DIPG-13 DIPG cell lines, respectively. DIPG tumor cells are fluorescently labeled with nuclear restricted GFP (green), endothelial cells are labeled with nuclear spirochrome dye, SPY650 (blue), and microglia are labeled with tagRFP (red).

96-well plates did not impact on the inherent ability of adherent stromal cell types and non-adherent DIPG cells in co-culture to promote cell-cell contact. The formation of 3D micro-tissue like structures in flat- and U-bottom 96 well platforms, has been subsequently utilized interchangeably to delineate DIPG cell behavior in the context of the stromal microenvironment.

High throughput cell culture tracking was used to perform a comparative analysis of co-culture parameters including initial cell density, cell combination, and culture platform (flat- or U-bottom) to investigate growth dynamics of the TTA spheroid assembly. Data from the tumor cell only (T) and heterogeneous suspension cultures of DIPG cells and Endothelial cells (TE) or Microglia (TM) in equal proportion with a total of 30,000 cells/well in Fig. 4B show that the presence of endothelial cells in co-culture with GFP-expressing DIPG cells is a key contributor to the formation of multicellular aggregates ( $>2000 \mu\text{m}^2$ , top) on 96-well flat bottom plates. These aggregates subsequently coalesced (Cluster area,

middle) overtime  $\sim 144$  h, promoting proliferation of the GFP-expressing DIPG cells (Tumor cell count, bottom). The pattern of spontaneous aggregation, coalescence, and subsequent expansion did not occur in a comparable manner when tumor cells were cultured alone (T) or in combination with microglia (TM) and no significant proliferation of tumor cells was observed over the period of 7 days of monitoring. Figure 4C displays the IncuCyte blended phase contrast/fluorescence images in real time for individual combinations of stromal cell types and/or GFP-expressing SU-DIPG-6 and SU-DIPG-13 cells (T) at the indicated cell densities and time points on 96-well low-attachment U-bottom plates. While all combinations formed a single spheroidal cluster by day 5, the sphere-forming potential of both GFP-expressing cell lines (SU-DIPG-6 and SU-DIPG-13) was enhanced between day 0-2 by the presence of RFP-expressing microglia (M) and/or endothelial cells (E). Snapshots of the 3D TTA comprising all three cell types (TEM) showed the formation of



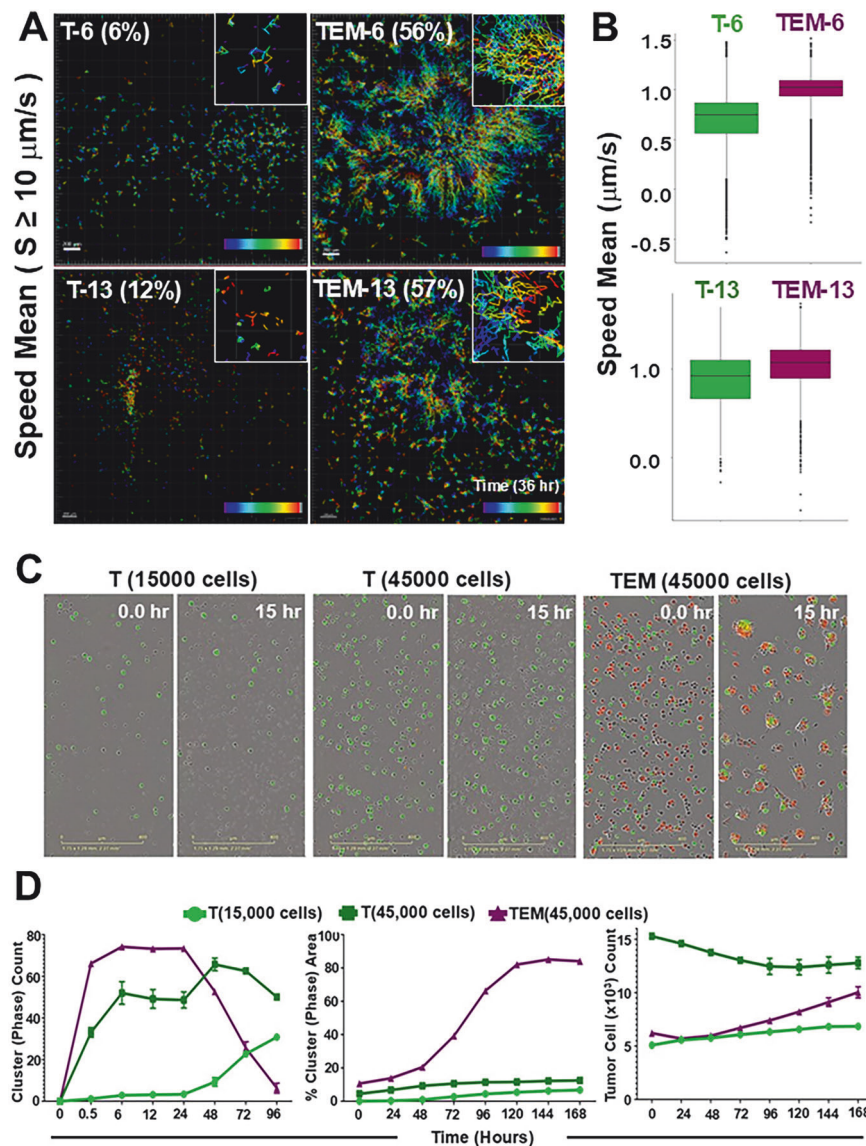


**Fig. 3** Tumor-stromal interaction influences motility and growth of DIPG cells in real time. **A** Snapshot of mean track speed (threshold  $S \geq 10 \mu\text{m/s}$ ), of DIPG cells (nuclear GFP; green) in “tumor cell only” (T-6 and T-13) and in co-culture (TEM-6 and TEM-13) condition with endothelial cells (SPY650 nuclear stain; blue) and microglia (nuclear tagRFP; red). Real-time live cell images were acquired at 30 min intervals over 28 h. Scale bar = 200/300  $\mu\text{m}$ . Time stamp for the tracks is color coded as indicated in each image (Purple-Blue-Green-Yellow-Red). A magnified (2.5X) region of each image is also included as an inset. **B** Corresponding quantitative track speed mean ( $\mu\text{m/s}$ ), length ( $\mu\text{m}$ ), displacement ( $\mu\text{m}$ ), and straightness (D/L) are plotted on a **Log10** scale. The differences in tracking parameters of GFP-expressing DIPG cells in the two culture conditions were significant at  $\alpha=0.05$ . **C** Representative Incucyte snapshots from real-time imaging at 0 and 15 h for nuclear restricted GFP-expressing SU-DIPG-6 cells alone (T) and in co-culture with endothelial cells and microglia (TEM). DIPG cells in T were plated at two separate densities (15,000 and 45,000 cells), corresponding to the T cell count in co-culture and the TEM total cell count, respectively. **D** Quantitative culture analysis of multicellular aggregates over a period of 5 days included cluster count (Left), cluster area (Middle; % normalized to cluster area above threshold at 0 h time Point), and tumor cell count (right). Applied cluster threshold for analysis = 2000  $\mu\text{m}^2$ .

compact spherical structures in each well with the process initiated within 24 h of incubation. The aggregation of DIPG cells alone in similar low adherent conditions of the U-bottom wells was gradual and they continued to remain as multicellular composites until day 2, even when incubated at increasing confluency of 15,000 [T(1)], 30,000 [T(2)] and 45,000 [T(3)] cells/well [T(1)]. Varying plating density for tumor cell only cultures was included in the experimental design to ensure that it was not the increase in the number of cells in the co-culture (TEM) but the presence of stromal cell types that influenced formation of a single spheroidal structure in the U-bottom well. All other combinations with (TE, TM) or without co-culture with DIPG cells (EM) formed a single compact spherical cluster by day 2. The

results provide support for the co-culture (TEM) acting as a 3D microtissue with behavior distinct from DIPG cell clusters alone and prompt the use of additional methodologies to gauge the ability of 3D TTAs to recapitulate the biological nature of DIPG tissue.

#### DIPG cells in the 3D TTA demonstrate improved correlation with activity of attempted therapeutic strategies compared to DIPG cells cultured alone

**Temozolomide (TMZ) chemotherapy.** Temozolomide is a traditional chemotherapy drug for high-grade glioma. The TMZ pharmacokinetics from two clinical trials ranged between 0.5 and 72  $\mu\text{M}$  in the plasma and 0.8–9.9  $\mu\text{M}$  in the cerebrospinal fluid (CSF) [47].

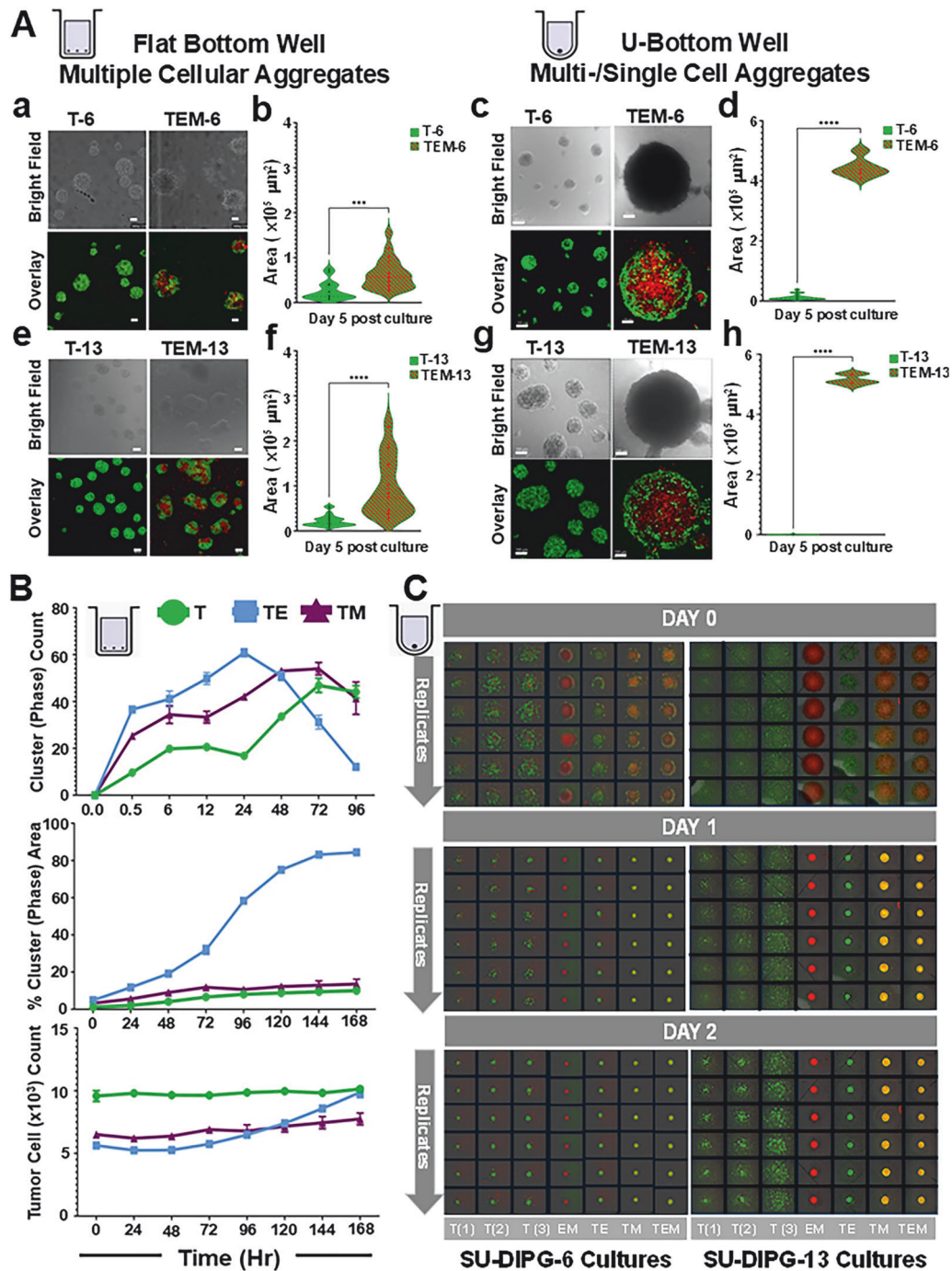


**Fig. 4 Human brain microvascular endothelial cells and microglia modulate the formation of multicellular aggregates in co-culture and influence the growth of DIPG cells.** **A** Representative bright field and fluorescence images of cultures on day 5 in 96-well flat-bottom (**A**, **C** and U-bottom **E**, **G** plates forming multi- and/or single cell aggregates. T-6 & T-13 denote neurospheres formed from tumor cells expressing nuclear restricted-GFP only (SU-DIPG-6 and SU-DIPG-13 cell lines, respectively; green). TEM-6 & TEM-13 denote 3D TTA comprised of DIPG cells (green), microglia (nuclear restricted tagRFP; red) and endothelial cells that do not carry any fluorescent label. Cluster area ( $\mu m^2$ ) calculated after measuring diameter in confocal images with the line tool of LAS X software and displayed as violin plots, for flat-bottom **B**, **D** and U-bottom **F**, **H** plates ( $n = 16\text{--}25$  per sample set; \*\*\*\*  $p < 0.0001$ ). Scale bar = 100  $\mu m$ . **B** Growth metrics from live cell imaging in 96-well flat-bottom plates with tumor (GFP-expressing DIPG-6) and stromal cell types incubated in different combinations and cell density are displayed over time, including number of aggregate clusters (cluster threshold = 2000  $\mu m^2$ ) (Top), cluster area (Middle), and tumor cell count (Bottom). Neurosphere formation by tumor cell only cultures at 30,000 cells/well [T(2)] served as control, in comparison to tumor:endothelial cell (TE) and tumor:microglial cell (TM) combinations. **C** Overlay of phase contrast and fluorescence images (Incucyte) of multicellular aggregation in 96-well U-bottom plates using two DIPG cell types, with variable plating density and variable cell combinations of Tumor, Endothelial, and Microglial cell cultures, monitored over time (Day 0–2 d). The annotations denote: T(1): 15,000 cells/well; T(2), EM, TE, TM: 30,000 cells/well and T(3), TEM: 45,000 cells/well.

TMZ alone or in combination with radiation has proven to be of low efficacy in pediatric patients with DIPG and in patient-derived *in vivo* models [48, 49]. We used TMZ drug titration ranging between 0 and 400  $\mu$ M to demonstrate the utility of *in vitro* 3D cell culture for rapid translation of clinically relevant response of chemoresistance in DIPG. Using real-time quantitative live-cell imaging and analysis platform, we compared the response of DIPG cells as neurospheres or in 3D TTA co-culture to a TMZ dose range of 0–400  $\mu$ M (Fig. 5A, B). TMZ concentrations from 0–100  $\mu$ M did not affect DIPG-6 cell viability or proliferation in the two culture conditions, as assessed by tracking the GFP-expressing tumor cells. Inability of the lowest tested dose of 25  $\mu$ M, which is far above the plasma/CSF concentration of TMZ, to elicit a cytotoxic effect in the DIPG cells is indicative of their resistance to TMZ. Figure 5B shows that incubation of 3D TTA with TMZ at 400  $\mu$ M reduced cell viability of GFP-expressing DIPG-6 (TEM-6) by only ~20% at 72 h, while a reduction in viability of ~60% was observed for tumor cells cultured alone (T-6). These results suggest that stromal influence augments the therapeutic resistance to TMZ in DIPG cells. D54, a patient-derived GBM cell line, generated from a 53 year old adult male, originally reported to be sensitive to TMZ [50] served as a positive control for this experiment. Supplementary Fig. 5 demonstrates inhibition of tumor cell viability by 80% in D54 cells at 50  $\mu$ M TMZ concentration by 72 h in this cell line.

**Panobinostat and marizomib:** The oral histone deacetylase (HDAC) inhibitor, panobinostat, and small molecule proteasome inhibitor, marizomib, have been screened as potential therapeutics in pre-clinical and clinical investigation for DIPG [51–53]. The effect of 0–32 nM of either drug on 3D TTA was analyzed over 96 h by real-time quantitative live cell imaging (Fig. 5C, D & Supplementary Fig. 6). GFP-expressing tumor cells in the 3D TTA (T-TEM-6 and T-TEM-13, blue dotted and solid line) demonstrated increased resistance to higher concentrations of both drugs in comparison to neurosphere cultures of tumor cells alone (T-6 and T-13, green dotted and solid line) in Fig. 5C. Notably, RFP-expressing microglia in the 3D TTA did not exhibit significant change in cell viability over 96 h at the indicated concentrations of drugs represented as M-TEM-6 and M-TEM-13 (grey dotted and solid line) in Fig. 5C. The raw values for each experiment were normalized as percentage to the total starting number of untreated cells.

**Dinutuximab anti-GD2 immunotherapy:** GD2-targeting has been identified as a potential immunotherapeutic approach for multiple cancers including DIPG [12]. Immunotherapy with Dinutuximab is thought to promote anti-tumor-effects by activating the innate immune microenvironment. Figure 6A provides a schematic of the components of the innate immune system that can be activated or tamed by a monoclonal antibody immunotherapy that targets potential GD2 antigens on tumor cells. Using flow cytometry, we found GD2 to be highly expressed on the surface of several DIPG cell lines (SU-DIPG-6, SU-DIPG-13, SU-DIPG-17 and SF8628), except for SU-DIPG-4 that we investigated (Fig. 6B). GD2 expression in SU-DIPG-17, -13, and -6 was notably higher than that in medulloblastoma (UW-228-2), adult glioblastoma (GBM, D54) and neuroblastoma (CHLA-15, 9464D) cell types. Human CHLA-15 and murine 9464D neuroblastoma cell lines were included as positive controls, and the L-AN-6 neuroblastoma cell line served as a negative control. We observed dinutuximab (0.5  $\mu$ g/ml)-mediated cytotoxicity of SU-DIPG-6 cells alone and in 3D TTA in the presence of human plasma obtained from healthy donors (10%). Tumor cell killing in both the tumor cell-only and 3D TTA co-cultures in the presence of human plasma with complement proteins was very rapid and occurred within 3–9 h of dinutuximab antibody addition (Fig. 6C, D). The DIPG cells in 3D TTA (TEM) underwent cytotoxicity by an additional ~50% compared to tumor cells alone incubated at low and high cell density with dinutuximab. The 3 and 9 h time-point post-treatment were selected to demonstrate sensitivity of DIPG cells in the 3D TTA to

dinutuximab via complement and microglial activation. The RFP-expressing microglia in co-cultures remained unaffected by the treatment. The cytolytic effect of dinutuximab was not observed with heat-inactivated human plasma (HI-HP). Data for each treatment condition was averaged from 4 wells in the Incucyte S3 system ( $p < 0.05$ ). In Fig. 6E, we incorporated microglia maintained in 40% human serum to form 3D TTA comprised of activated microglia to induce antibody-dependent cell-mediated cytotoxicity. The presence of activated microglia resulted in ~20% reduction in cell viability at 3 h treatment with dinutuximab (0.5  $\mu$ g/ml). To permit a comparison across drug-treated experimental replicates, the viable cell count values for each experiment were normalized by setting the value of untreated cells at 100% and by converting each raw cell count value to a percent of untreated control.

### The integrated omics landscape of 3D TTA reveals the impact of tumor ecosystem on gene expression sharing features with the Glioma/GBM tissue phenotype

We utilized high throughput omic techniques to probe the molecular changes that result from DIPG co-culture in the 3D TTA model. Pan-analysis by mass spectrometry, presented as a Volcano plot (Fig. 7A), identified a total of 4085 proteins in the cellular proteome (cell pellet) and 503 proteins in the secretome (supernatant) of the 3D TTA and corresponding SU-DIPG-6 cell-only neurospheres collected at day 5, 10 and 15 post-culture, with 50% medium change every 48 h. Of these, 229 proteins were up-regulated, and 179 proteins were down-regulated in the cellular proteome of the 3D TTA in comparison to the DIPG cell-only cultures (Supplementary Material Excel\_Proteomics). Differential expression of these proteins was plotted based on a significance of  $-\log_{10} p \geq 1.3$  and a fold-change represented on  $\log_2$  scale that was  $\geq$  or  $\leq 1.5$ . For the secretome, which was partially replenished every 2 days and final collected for analysis on day 5, the applied threshold of  $\log_2$  fold change was reduced to  $\geq$  or  $\leq 1.2$ , to account for the anticipated impact of successive medium change on prevalence of proteins in the supernatant. The data showed upregulation of 31 proteins and downregulation of 30 proteins (Fig. 7A).

Fig. 7B provides the RNA-Seq transcriptomic volcano plot indicating the overall extent of differential gene expression for flow-sorted DIPG cells in the 3D TTA (combined results from TEM-6 [Biological coefficient of variance (BCV) 0.113] and TEM-13 [BCV 0.071] compared to DIPG cell-only cultures (T-6 [BCV 0.069]) and T-13 [(BCV 0.046)] (Supplementary Fig. 8B). RNA-Seq analysis identified 1100 genes with a log-fold change greater or less than 1.0 and a false discovery rate (FDR)-corrected p-value less than 0.05. Of these, 349 were down-regulated and 751 were up-regulated among the two cell types, as illustrated in the volcano plot. The differentially expressed genes and proteins were screened by gene set enrichment analysis for functional significance. Heat maps were created from the set of 11 statistically significant proteins/genes that demonstrated a similar expression profile by proteomic and transcriptomic analyses, utilizing variance stabilizing normalization (VSN) (Fig. 7C, D). Identified genes included TIMP1 (tissue inhibitor of metalloproteinase-1), COL6A1 (Collagen Type VI Alpha 1 Chain), LGALS1 (Galectin-1), LGALS3 (Galectin-3), SOD2 (Superoxide Dismutase), CLIC1 (Chloride Intracellular Channel 1), STAT3 (Signal transducer and activator of transcription 3), CEBPB (CCAAT Enhancer Binding Protein Beta), ITGA5 (Integrin Subunit Alpha 5), PLSCR1 (Phospholipid scramblase 1) and MVP (Major Vault Protein). Notably, the identified gene set included NFKBIZ (NFKB Inhibitor Zeta), VCAM1 (Vascular Cell Adhesion Molecule 1) and CCL20/ MIP-3 $\alpha$  (C-C motif chemokine ligand 20 or macrophage inflammatory protein-3  $\alpha$ ) (Fig. 7D, red), which are functionally related to the intracellular signaling network from nucleus to cell surface (Fig. 7D, E).



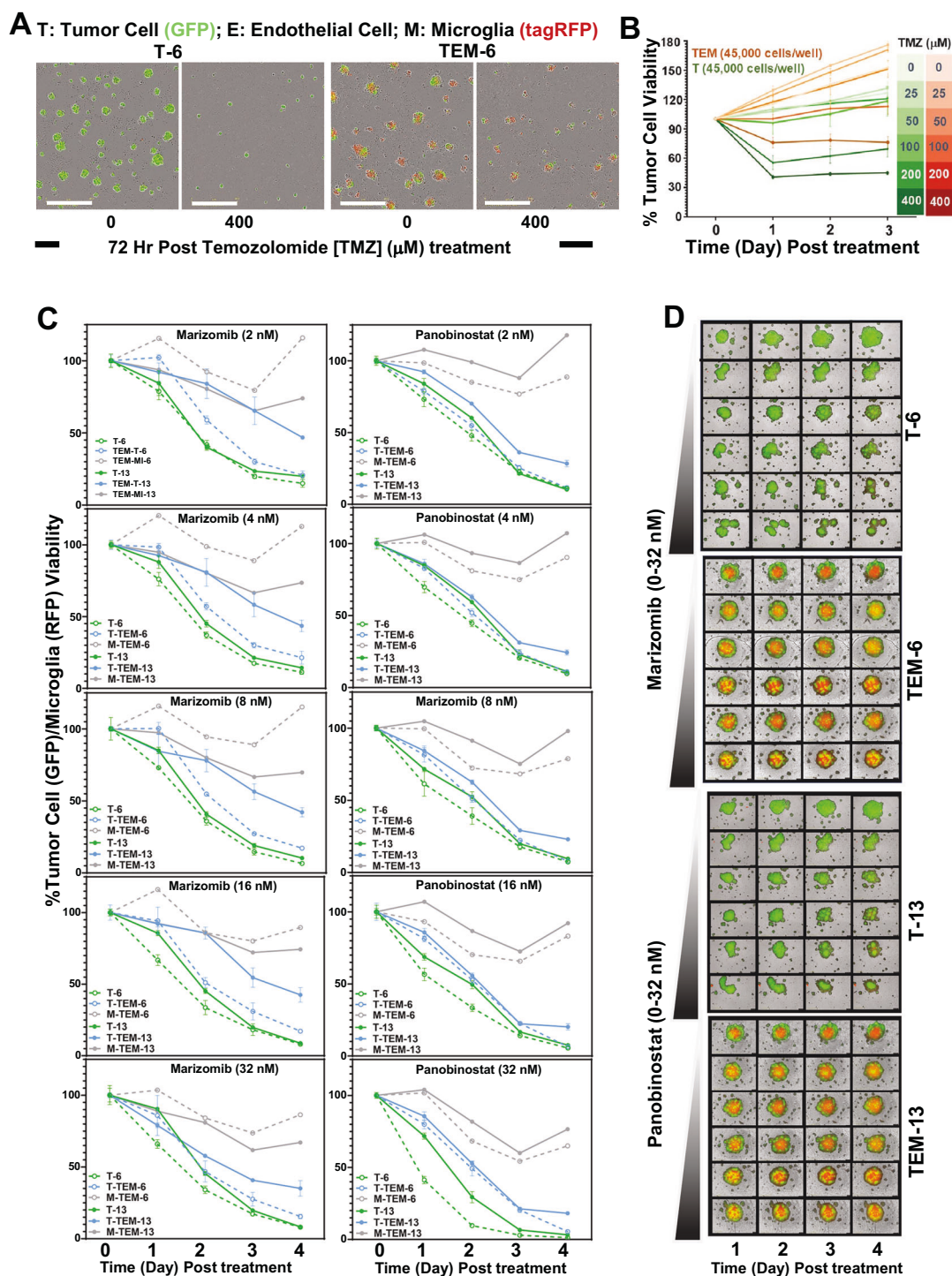


**Fig. 5** DIPG cells are protected from chemo- and targeted-therapies by the presence of stromal cell types. **A** Representative images demonstrating response to TMZ chemotherapy (400  $\mu\text{M}$ ) in GFP expressing SU-DIPG-6 tumor cells (T-6) alone and in 3D co-culture with microglia expressing tagRFP and endothelial cells with no fluorescent marker (TEM-6) at 72 h post treatment in flat-bottom 96-well plates. **B** % tumor cells present over time for GFP-expressing DIPG cells alone (green) and in 3D co-culture (orange) after treatment with variable concentration of TMZ (0–400  $\mu\text{M}$ ). **C** Quantification of cellular growth in U-bottom 96-well plates and **D** corresponding representative IncuCyte images (T-6, T-13 and TEM-6, TEM-13) demonstrate response to variable concentration of Marizomib (0–32 nM) and Panobinostat (0–32 nM) from 1–4 days. Here the tumor cells express GFP fluorescence (Green) and microglia express tagRFP (red) and endothelial cells do not express any fluorescent protein. Response of SU-DIPG-6 and SU-DIPG-13 tumor cells alone is identified as T-6 and T-13, respectively (green solid and dotted line). Response of GFP-labeled tumor cells in TEM-6 and TEM-13 co-culture with microglia and endothelial cells is denoted as T-TEM-6 and T-TEM-13 (blue solid and dotted line). Response of microglia (quantified via tagRFP label) in TEM co-cultures is indicated as M-TEM-6 and M-TEM-13 (Grey dotted and solid line). In all cases, values of integrated green- or red- fluorescence intensity per well (from GFP and tagRFP expression) were averaged across 4 well replicates per experiment.

DIPG/DMG is a rare malignancy with limited information and access to surgical tissue biopsies [54]. To investigate the significance of the set of genes/proteins identified by the integrated omic analysis, we interrogated open-access public database of The Cancer Genome Atlas (TCGA) and The Human Protein Atlas (THPA) in the context of glioma patients to assist in the evaluation of attributes specific to the in-situ brain tumor tissue in our experimental model. The correlation indicates the impact of stromal influence on changes associated with oncogenic signaling in DIPG cells. TCGA data correlating survival probability in GBM/glioma patients with RNA expression showed that overexpression of each of the identified genes (except for VCAM1) was associated with poor prognosis (Supplementary Fig. 7). We explored data from THPA for relative expression of the identified proteins in GBM/glioma patient tissue samples compared to reference samples of normal brain tissue (Fig. 7G, H). Digital immunohistochemical analysis from 10–14 patient samples revealed significantly increased expression of 9 proteins in tumor tissues when compared to the normal brain tissues, which included STAT3, SOD2, CEBP, ITGA5, MVP, LGALS1, CLIC1, LGALS3 and VCAM1. Five (CEBPB, PLSCR1, COL6A1, TIMP1 and NFkB1Z) of the 14 candidate proteins overexpressed in the 3D TTA model did not demonstrate any significant change in the glioma/GBM cohorts, suggesting that DIPG/DMG may express molecular characteristics distinct from those in the general glioma/GBM tumors. Thus, capturing features of the disease-specific TME by including interacting cell-types in the 3D TTA is associated with alterations in genomic expression.

#### Gene set enrichment analysis reveals that tumor-stroma interactions alter vital biological processes in DIPG cells

The Gene Ontology (GO) knowledgebase was used to perform enrichment analysis on the four different RNA seq datasets obtained from SU-DIPG-6 and SU-DIPG-13 cultures, comparing tumor cells cultured alone with those co-cultured with stromal cell types in the 3D-TTAs. This omics data-driven approach identified differentially expressed genes involved in biological processes captured with GO terms: (i) microenvironment signaling; (ii) DNA replication and damage; and (iii) immune regulation. Unsupervised gene set enrichment analysis was performed with the Ingenuity Pathway Analysis (Qiagen) to reveal statistically significant pathways (Supplementary Fig. 8) including those defined via GO. Data are presented as RPKM (i.e. the number of reads per kilobase of transcript divided by the number of all reads mapped in millions) heatmaps in Fig. 8A–C. Corresponding directed acyclic graphs of gene and protein-protein interactions were constructed (Fig. 8D, E). The upregulated expression of MHC related genes on tumor cells when in co-culture with stromal cell types (TEM) in Fig. 8A, B is an interesting finding that indicates the potential of tumor-stromal cell co-culture as a promising strategy to enhance the efficacy of immunotherapy. The list of perturbagens including small molecules, pharmacologic and biologic was obtained via CMap analysis (Supplementary Material-Excel-CMap). The top 10 chemical perturbagens predicted by the connectivity maps with the highest negative enrichment scores predicted to generate opposite gene expression included inhibitors for Aurora kinase A, C-Jun N-terminal kinase (JNK), Protein kinase C (PKC), transforming growth factor beta (TGF- $\beta$ ) receptor and Calcineurin as presented in Supplementary Fig. 9.

#### DISCUSSION

The tumor tissue can be described as an evolving ecosystem. Interactions between neoplastic and non-neoplastic cells in a developing tumor influence the TME, which in turn reprograms cancer cells to promote survival or resistance to therapy [55, 56]. Investigating these interactions to unravel the complex

interplay between proliferation, invasion and therapeutic resistance of cancer cells requires developing representative surrogate platforms. Acquisition of autopsy specimens for research has enabled the development of orthotopic patient-derived xenograft mouse models that manifest the patient tumor heterogeneity [57], and the generation of treatment-resistant DIPG/DMG cell lines. These cell lines have served as experimental platforms providing meaningful insights into the molecular alterations driving malignancy [58]. This knowledge base has led to the generation of genetically engineered models that can be very useful to understand DIPG tumorigenesis in the brainstem of immune proficient mice and as valuable tools for pre-clinical testing [21–23]. Robust and reproducible in vitro studies followed by thorough validation in animal models has been routinely used for translation of findings or therapeutics to clinical settings. Nevertheless, a concordance between the preclinical studies and clinical trials has proven to be challenging for many diseases, including H3K27M-altered DMG/DIPG. Acknowledging the strengths of each of the preclinical DIPG/DMG models to understand progression of the disease and test potential treatments, we introduce an innovative methodology for generating a 3D co-culture model with potential to reproduce the intricate interplay between cancer cells and their surrounding micro-environment as a more reliable alternative for capturing tissue characteristics and preclinical testing in vitro before validation in the in vivo animal models. This cost-efficient approach is expected to augment the translational accuracy of drug development to pediatric trials and streamline the extensive use of animals in preclinical investigations.

#### Role of multi-cellular systems

Understanding the TME complexity in vitro requires simplifying approaches. A 'reductionist bottom-up approach' was selected to develop our in vitro 3D model. This study provides the rationale for the breakdown or reduction of the TME that can be successfully studied in the 3D TTA disease model for DIPG comprised of authenticated microvascular endothelial cells [59], microglia [60] and radiation-resistant DIPG cells of human origin. We propose here a 3D co-culture platform incorporating aspects of the TME as a cost effective and reproducible alternative, and more importantly, with the capacity to be experimentally manipulated. While in vitro models only approximate the biological reality of de novo human tumors, this platform was designed to generate a 'better approximation' of pediatric DIPG compared to tumor cells cultured alone, as gauged by morphology, functional growth behavior, genomic expression, and drug response, and to yield consistent results over multiple DIPG cell types. To establish our model, several co-culture methodologies were initially evaluated and suspension cultures in serum-free medium led to the reproducible formation of 3D multicellular aggregates with phenotypic endpoints for quantitative analysis and amenable to diverse experimental conditions. This work takes advantage of the capacity of multiple cell types in suspension to form 3D clusters, and investigates the influence of subsequent tumor-stromal interactions to generate a more representative in vitro model of tumor behavior. We demonstrate that stromal cell types play an important role in the architecture, growth behavior, genomic expression, and functional drug response of 3D TTA and the proliferation/organization of DIPG cells. As the model does not incorporate all components of the DIPG tissue, we have introduced the term 'Tumor Tissue Analogs' to designate such models [61, 62]. This 3D platform enables the subsequent addition of potentially contributing other tissue specific components of DIPG to improve our understanding of DIPG biology and preclinical evaluation of drug efficacy in patients.

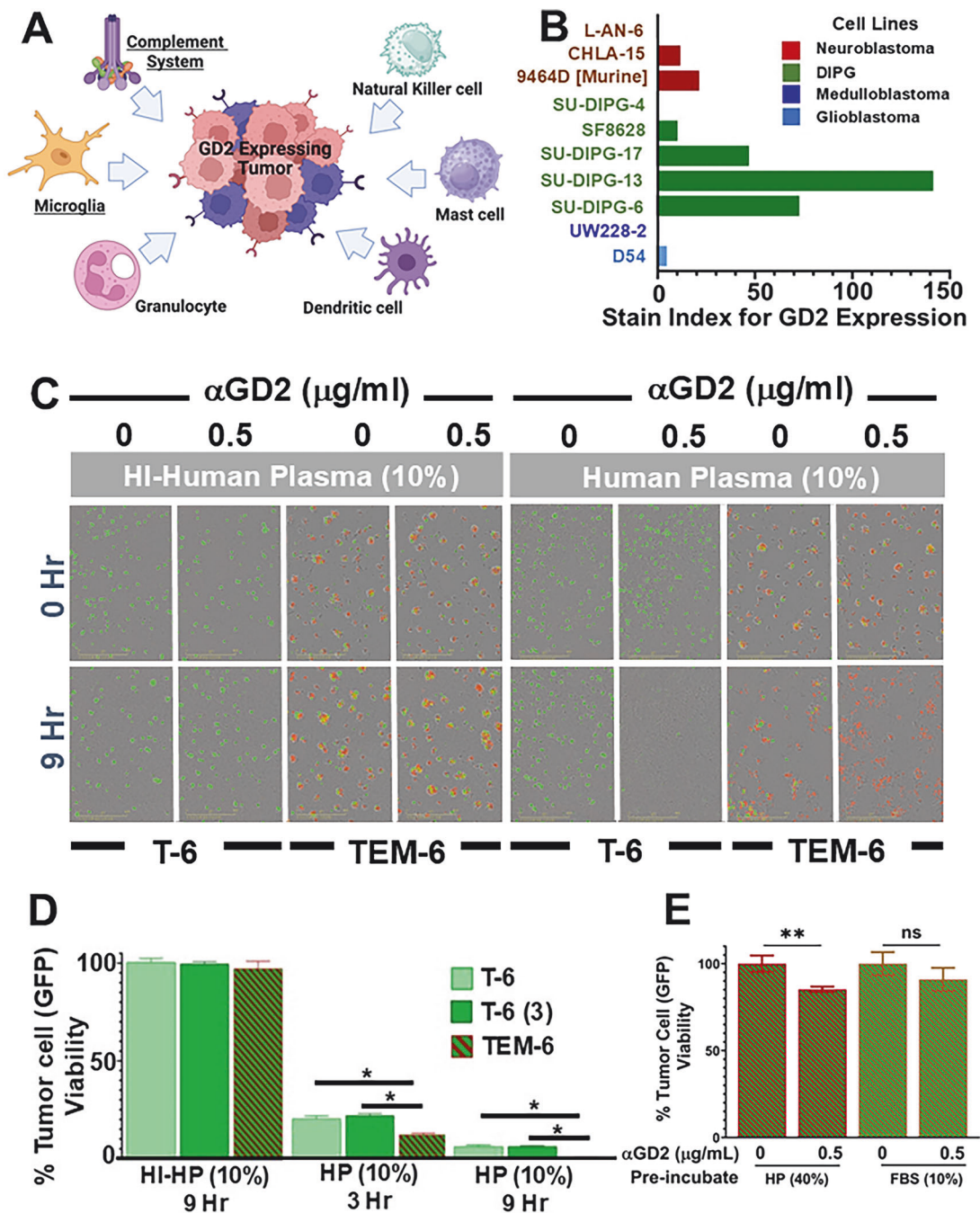


**Fig. 6** The presence of stromal cell types sensitizes DIPG cells to antibody-based immunotherapy. **A** Schematic demonstrating components of the innate immune system that can be exploited to target GD2-expressing tumors. Yellow highlighted complement system and microglia are investigated in the present 3D DIPG model. **B** Expression of the tumor specific disialoganglioside GD2 on the surface of patient-derived DIPG cell lines (green: SU-DIPG-4, SF8628, SU-DIPG-17, SU-DIPG-13, SU-DIPG-6), measured by flow cytometry with primary labeled GD2 APC (clone 14G2a) mAb. Stain Index (SI) for GD2 expression was normalized to isotype control (mouse IgG2a APC ab). Neuroblastoma cell lines (red: L-AN-6, CHLA-15 & 9464D) served as additional positive controls. Medulloblastoma (UW-228-2) and glioblastoma (D54) cell lines served as negative controls. **C** Representative images of DIPG-6 cells cultured alone as neurospheres (T-6) or in co-culture as TTA (TEM-6), shown after treatment with dinutuximab (14G2a) mAb in the presence of human plasma (10%) donated from healthy volunteers ( $n = 4$ ) as well as heat-inactivated human plasma (HI-HP; control) at 0 and 9 h. **D** Relative DIPG tumor cell viability (integrated GFP green fluorescence intensity per treated well normalized to average fluorescence intensity of untreated wells) at 3 h and 9 h, showing stromal influence on extent of antibody-based complement-dependent lysis of GD2 expressing DIPG cells plated in variable density [T-6, light green] and T-6(3), Dark green] and in combination with microglia and endothelial cells (TEM-6, Red-Green). Results were averaged across 4 well replicates per experiment. Statistical significance was determined by one-way ANOVA and Tukey post-hoc test. \*  $p$ -values < 0.05 for dinutuximab-induced cytotoxicity in GFP-expressing DIPG cells were defined significant. **E** DIPG-6 tumor cell viability in 3D TTA comprised of microglia preincubated in 40% human serum or 10% FBS at 3 h post-treatment with dinutuximab (0.5 μg/ml).



### Morphology, histology, and functional growth behavior

Confocal imaging, histology and functional loss of histone trimethylation of fluorescently labeled DIPG cells in co-culture with stromal cells capture the ability of non-adherent DIPG to self-organize with adherent stromal cell types into 3D tissue-like structures simulating aspects of the DIPG tissue biology (Fig. 1). The data obtained from spatiotemporal imaging by live cell tracking showed a notable increase in phenotypic measures of cell motility, including speed, length, displacement, and straightness of GFP-expressing DIPG cells under stromal influence versus those from tumor cell only cultures (Figs. 2, 3 and Supplementary Fig. 4). These findings suggest that the stromal microenvironment can spur migration or invasive behavior of tumor cells that is not evidenced from the tumor cell only cultures. This is in agreement with the ability of DIPG/DMG cells to infiltrate and spread into the healthy brain tissue, resulting in significant damage and a poor prognosis.

Emerging evidence from reports evaluating the immune microenvironment [63] and spatial analysis of receptor-ligand candidates in DIPG-infiltrated brainstem [64] indicate the active involvement of the endothelial and myeloid populations, specifically the microglia via crosstalk with the cancer cells that promote tumor progression. Our study supports these findings and reveals the ability of endothelial cells to promote the self-assembly of TTA and proliferation of DIPG cells in co-culture (Fig. 4). Future work will concentrate on understanding the molecular underpinnings of the observed phenomenon.

### Drug response

The therapeutic options for DIPG have remained unchanged over several decades. Radiation therapy (RT), the standard treatment for DIPG, is merely palliative as it only extends survival by approximately 3 months [65]. The SU-DIPG-6 and SU-DIPG-13 cell lines used in this study are derived from H3.3 K27M-altered DMG autopsy samples of patients that have undergone radiation treatment, exhibiting stem-like characteristics known to contribute to the aggressiveness of the cancer [66, 67]. Therefore, as these cell lines are radiation-resistant, we have investigated the responses to second line treatments. Traditional, targeted and immunotherapies that are in clinical/preclinical trials were chosen to demonstrate the utility of the 3D TTA in evaluating the therapeutic response.

TMZ is a well-studied chemotherapeutic drug for high-grade glioma [68] that is cytotoxic to DIPG cells in vitro, but has not been shown to have any clinical therapeutic efficacy in pediatric patients with DIPG [69, 70]. Typical TMZ pharmacokinetic data in adult patients with high-grade glioma showed active concentrations of 0.5–72  $\mu$ M in plasma and 0.8–10  $\mu$ M in cerebrospinal fluid [47]. Stromal influence in the 3D TTA increased the in vitro resistance of DIPG cells to TMZ, even at concentrations as high as 400  $\mu$ M (Fig. 5A, B), confirming the lack of efficacy in patients [48, 71]. Recent investigations have indicated that HDAC and/or proteasome inhibitors may be effective against multiple neoplastic cell types, including DIPG [53, 72, 73]. We selected the HDAC inhibitor panobinostat and small molecule proteasome inhibitor marizomib for testing in the 3D TTA. Comparing DIPG cells alone to those in 3D TTA showed reduced tumor sensitivity to the two drugs in the TTA (Fig. 5C, D and Supplementary Fig. 6), similar to the outcomes from clinical trials in glioblastoma patients [74, 75]. Both panobinostat and marizomib are designed to specifically target and kill cancer cells. We did not observe any change in the viability of the RFP-expressing microglia at the drug concentrations studied, confirming the cancer cell-specific targeting in the heterotypic co-culture of 3D TTA.

Antibody-based targeting is a form of cancer immunotherapy that facilitates cancer cell recognition by the innate immune system. Microglia and a set of complement proteins

circulating in the blood are components of the innate immune system known to play a role in the disease course of several central nervous system pathologies. Cancer cells are often capable of escaping this mechanism of immune surveillance. When coated with tumor-specific antibodies, the cancer cells are readily recognized as foreign and attacked by the innate immune system. The GD2 antigen is a disialoganglioside specifically expressed on several cancer cell types (Fig. 6A). Dinutuximab, is a chimeric antibody that is in clinical use, particularly for the treatment of high-risk neuroblastoma [76]. The antibody targets tumors expressing the GD2 antigen and effectively marks them for destruction by the patient's own immune system driven by the process of complement-dependent cytotoxicity (CDC) and antibody-dependent cellular cytotoxicity (ADCC) [77]. We evaluated this immunotherapeutic strategy by introducing human plasma in the 3D TTA model, and activating the innate immune microenvironment of the complement system in the human plasma and microglia using the GD2-targeting dinutuximab antibody (Fig. 6C, E). The data demonstrate that DIPG cells under stromal influence, particularly activated microglia, were sensitized to such targeting, in addition to the complement-induced killing via the GD2 specific dinutuximab antibody. This approach shows the potential of the 3D co-culture platform for investigating the functionality of specific tumor-immune interactions of clinical relevance, such as the human complement system and/or microglia, which may have been missed with existing immune compromised animal models or traditional cell culture methods.

### Genomic expression

The new co-culture model presented distinct spatio-temporal characteristics and therapeutic response with known agents when compared to 3D tumor cell spheroids. Integrated omics analyses by mass spectrometry and RNA sequencing (Fig. 7) comparing the DIPG cells in the 3D TTA with those cultured alone unveiled the reprogramming of the tumor cell circuitry by the surrounding stromal microenvironment. A set of 14 proteins/genes over-expressed in DIPG cells from the 3D TTA were identified that we curated into a non-canonical oncogenic signaling pathway in DIPG cells induced by Tumor:Stroma Interactions (Fig. 7E). These have been associated with shortened survival in glioma/GBM patients (via TCGA database, Supplementary Fig. 7). Immunohistochemical analysis from the public THPA database of malignant glioma/GBM specimens correlated with the elevated expression of these proteins in the 3D TTA (Fig. 7F, G). Literature-curated evidence from glioma/GBM studies on overcoming therapeutic resistance to TMZ and immune suppression by targeting some of the differentially expressed molecules identified via the integrated protein and RNA profiling in this study is provided in Supplementary Table 1. Functional enrichment analysis of the RNA sequencing data has provided associative-gene networks of microenvironment signaling, DNA replication & damage and immune regulation that are active in tumor cells of the 3D TTA (Fig. 8). The data show the ability of 3D TTA to capture these TME interactions that would have been difficult to identify using 2D/3D tumor cell only cultures. Many tumors evade immune surveillance by downregulating MHC-I, making them less visible to the immune surveillance by T cells. Restoration of expression of MHC-related genes in tumor cells of the TEM as observed in Fig. 8E, indicates that 3D model is a good platform to investigate and develop T-cell mediated immunotherapies in vitro. Furthermore, as described in the literature, some of these proteins could represent therapeutic targets (Figs. 7, 8); these include FDA-approved drugs such as atovaquone, an antimicrobial drug identified as a novel STAT3 inhibitor [78]; biguanides including metformin for blocking CLIC-1 [79]. Other drugs in clinical trials include BBI608 (Napabucasin), a small molecule inhibitor of STAT3

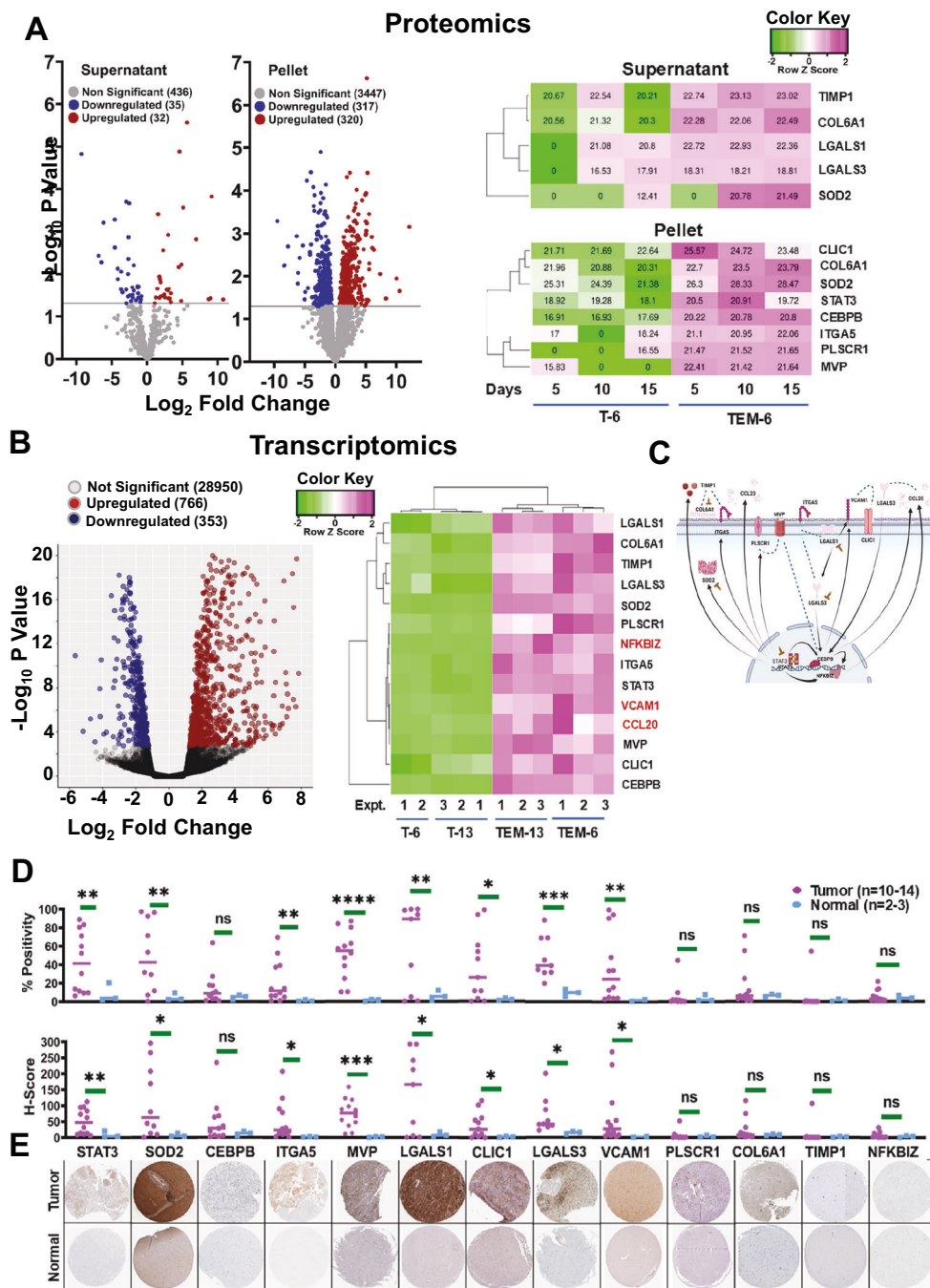


**Fig. 7 Integrated proteomic and transcriptomic analysis reveals the molecular influence of stromal cell types in the DIPG model.** **A** Volcano plots display p-values of proteins differentially expressed in TTA (TEM-6) versus DIPG-only neurospheres (T-6) (expressed as  $-\log_{10}$  p Value), plotted against  $\log_2$  fold change. Data from pellet (left) and supernatant (right) are presented separately. Mass spectrometric data was pooled over cultures at multiple points in time (5, 10, and 15 days of culture). Red data points indicate proteins with a p-value  $< 0.05$  and a  $\log_2$  fold change  $\geq$  or  $\leq 1.5$ . Grey data points have  $p > 0.05$ . **B** RNA seq analysis as  $-\log_{10}$  of the false discovery rate (FDR) for differentially expressed transcripts in flow-sorted GFP-expressing DIPG cells (TEM-6 –13 combined vs. T-6 –13 combined) plotted against  $\log_2$  fold change at day 5. Red data points indicate differentially expressed genes with FDR  $< 0.05$  and  $\log_2$  fold change  $\geq$  or  $\leq 1.0$ . Grey data points have FDR  $> 0.05$  and are not significant in the sample sets compared. **C** Heatmap visualization and hierarchical clustering of differential expression in select proteins identified by mass spectrometric analysis in the supernatant and pellet of TTA (TEM-6) and tumor cell-only cultures (T-6) (results shown from 5, 10, and 15 days in culture). **D** Heatmap visualization of the directed gene set in flow-sorted DIPG cells that are statistically significant (black) and also contribute to pathway enrichment (red) observed by RNA seq analysis. Data displayed are from GFP-expressing DIPG cells from the TTA (TEM-6 & TEM-13 shown independently) and GFP-expressing DIPG cells cultured alone as neurospheres (T-6 & T-13). Color key illustrates the relative expression across all samples. **E** Schematic representation of potential interactions among the differentially expressed select genes/proteins from the proteomic and transcriptomic datasets. **F** Scatter plots of relative staining positivity (% positivity) and histology score (H-score) analyzed from banked human glioma tissue samples (purple) and reference normal tissue samples (blue) from The Human Protein Atlas public database, pertaining to the identified transcripts. p-values from the omics datasets are identified as \*\*\*\* $p \leq 0.0001$ , \*\*\* $p \leq 0.001$ , \*\* $p \leq 0.01$ , \* $p \leq 0.05$ , identified as described above. **G** Representative 1 mm diameter immunohistochemical slices from glioma/GBM (Upper panel) and normal brain tissue (Lower panel) from THPA were used to perform the quantitative analysis in F.

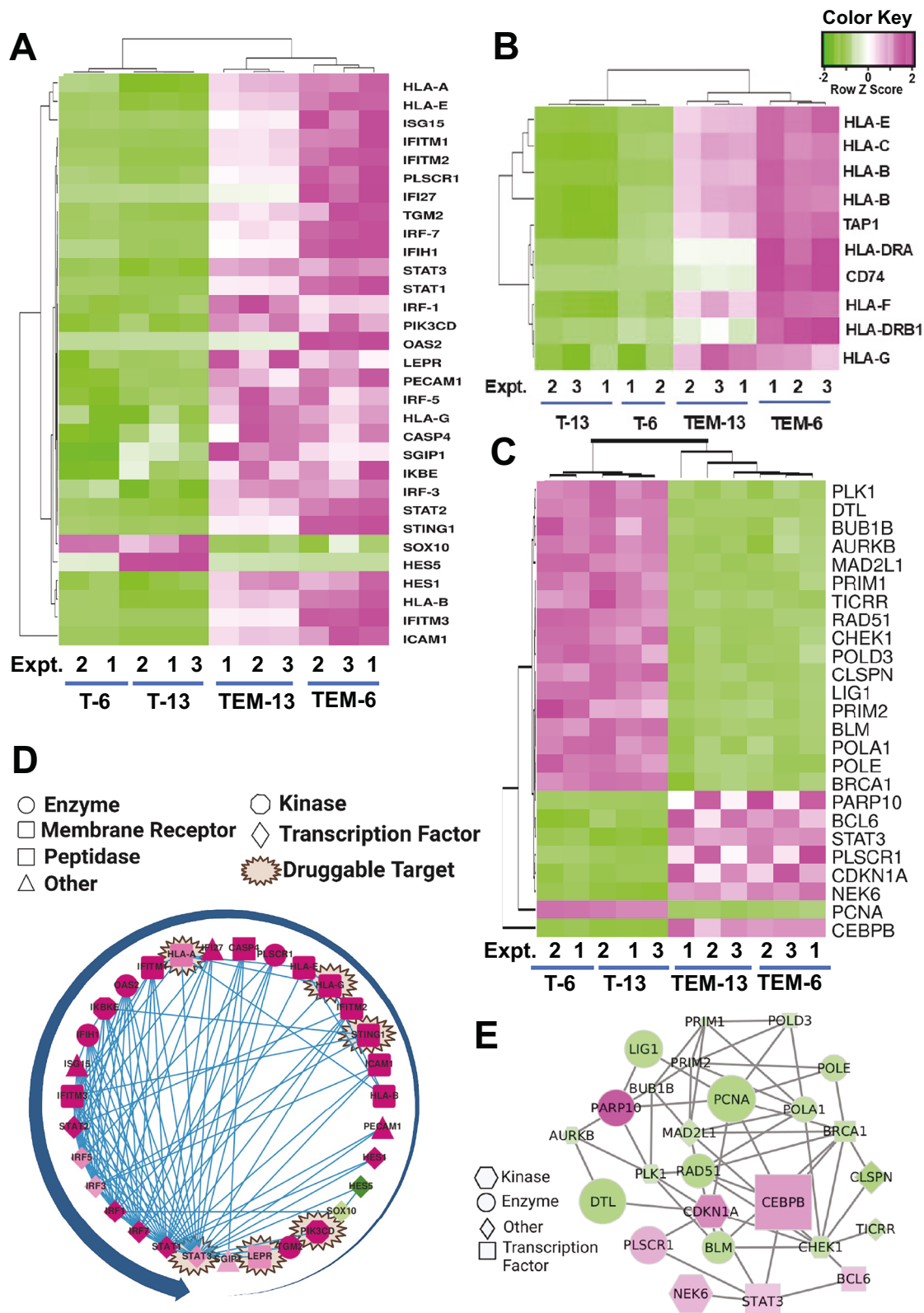


**Fig. 8** Gene Ontology analysis for enrichment of gene sets from transcriptomic data reveals the influence of tumor-stroma interactions on biological processes essential to microenvironment signaling, antigen presentation/processing and with DNA replication and damage in DIPG cells. **A, B, C** Heatmaps and **D, E** respective network abstraction for A and C (generated using Cytoscape) illustrate differential expression profiles of genes and their association for SU-DIPG-6 and SU-DIPG-13 cells collected from TTA (TEM-6 & TEM-13) and tumor cell only neurospheres (T-6 & T-13). Transcriptomic heatmap and identified network groupings are based on results from gene set enrichment (GSEA) and ingenuity pathway (IPA) analysis: **A, D** pertain to interferon and Tumor microenvironment signaling [GO: 0051240], **B** relate to antigen processing and presentation [GO: 0019882], and **C, E** relate to DNA replication and damage [GO: 0006259].



for advanced cancers [80]; and GB1211, an oral inhibitor of Galectin-3 in the treatment of fibrosis [81].

Preclinical research in neuro-oncology, including in DIPG, has mainly relied on animal models for validation of interactions between tissue-specific cell types [25, 26, 82]. Patient-derived DIPG cell lines from autopsy samples have been used for testing drug candidates in vitro [53]. Modern neuronavigation tools in surgery now allow access to biopsy specimens for generating treatment-naïve DIPG cell lines for preclinical studies [52]. Emerging biomimetic approaches utilizing Hydrogels [83] and induced pluripotent stem cells [84] as 3D in vitro models offer great promise for studying human brain tumor biology and drug screening. Nevertheless, the miniaturized 3D in vitro platform presented here mimics the critical microenvironment characteristics of pediatric DIPG and allows controlled experimental manipulations of difficult-to-study intercellular interactions. This platform with potential to be continuously refined by sequential addition of other stromal components, offers a compelling alternative to 2D cell culture as advancements in imaging, informatics, and molecular techniques allow for a wider range of investigations.

Representative and reproducible DIPG disease models are anticipated to improve patient outcome by assisting in accurate prediction of therapeutic response to drugs in development. A prudent approach would be to include a robust 3D co-culture method as described here to improve the selection of new therapeutic targets before pre-clinical assessment in representative animal models. Harnessing the 3D TTA to complement the existing and emerging physiologically relevant models in addressing provocative basic, translational, and clinical questions that provide meaningful and predictive insights into the underlying mechanisms and therapeutic response will accelerate the efficacy of ongoing and future clinical trials in DIPG/DMG. Building upon the findings, future work includes expanding the current research to investigate the standard radiation treatment alone and in combination with emerging therapeutic efforts including those aimed at exploiting the immune functions of this malignancy utilizing our 3D TTA generated from treatment naïve and treatment resistant cancer cell lines.

## DATA AVAILABILITY

The data of the respective dataset in the study may be obtained by reaching out to the corresponding author(s). Details for accessing the proteomics and RNA sequencing data are provided in the supplementary material.

## REFERENCES

- Hoffman LM, Veldhuijzen van Zanten SEM, Colditz N, Baugh J, Chaney B, Hoffmann M, et al. Clinical, Radiologic, Pathologic, and Molecular Characteristics of Long-Term Survivors of Diffuse Intrinsic Pontine Glioma (DIPG): A Collaborative Report From the International and European Society for Pediatric Oncology DIPG Registries. *J Clin Oncol*. 2018;36:1963–72.
- Tosi U, Souweidane M. Fifty years of DIPG: looking at the future with hope. *Child's Nerv Syst ChNS*. 2023;39:2675–86.
- Caretti V, Bugiani M, Freret M, Schellen P, Jansen M, van Vuurden D, et al. Subventricular spread of diffuse intrinsic pontine glioma. *Acta Neuropathol*. 2014;128:605–7.
- Qin EY, Cooper DD, Abbott KL, Lennon J, Nagaraja S, Mackay A, et al. Neural Precursor-Derived Pleiotrophin Mediates Subventricular Zone Invasion by Glioma. *Cell*. 2017;170:845–859.e819.
- Srikanthan D, Taccone MS, Van Ommeren R, Ishida J, Krumholtz SL, Rutka JT. Diffuse intrinsic pontine glioma: current insights and future directions. *Chinese Neurosurg J*. 2021;7:6.
- Hayashi A, Ito E, Omura M, Aida N, Tanaka M, Tanaka Y, et al. Hypofractionated radiotherapy in children with diffuse intrinsic pontine glioma. *Pediatrics Int*. 2020;62:47–51.
- Rechberger JS, Lu VM, Zhang L, Power EA, Daniels DJ. Clinical trials for diffuse intrinsic pontine glioma: the current state of affairs. *Child's Nerv Syst ChNS*. 2020;36:39–46.
- Vitanza NA, Monje M. Diffuse Intrinsic Pontine Glioma: From Diagnosis to Next-Generation Clinical Trials. *Curr Treat Options Neurol*. 2019;21:37.
- Morales La Madrid A, Hashizume R, Kieran MW. Future Clinical Trials in DIPG: Bringing Epigenetics to the Clinic. *Front Oncol*. 2015;5:148.
- Bailleul Q, Rakotomalala A, Ferry I, Leblond P, Meignan S, Furlan A. The art of war as applied to pediatric gliomas: Know your enemy. *Med Sci*. 2021;37:159–66.
- Lin C, Smith C, Rutka J. Current immunotherapeutic approaches to diffuse intrinsic pontine glioma. *Front Genet*. 2024;15:1349612.
- Majzner RG, Ramakrishna S, Yeom KW, Patel S, Chinnasamy H, Schultz LM, et al. GD2-CAR T cell therapy for H3K27M-mutated diffuse midline gliomas. *Nature*. 2022;603:934–41.
- Bender S, Tang Y, Lindroth AM, Hovestadt V, Jones DT, Kool M, et al. Reduced H3K27me3 and DNA hypomethylation are major drivers of gene expression in K27M mutant pediatric high-grade gliomas. *Cancer Cell*. 2013;24:660–72.
- Lewis PW, Müller MM, Koletsky MS, Cordero F, Lin S, Banaszynski LA, et al. Inhibition of PRC2 activity by a gain-of-function H3 mutation found in pediatric glioblastoma. *Science*. 2013;340:857–61.
- Johung TB, Monje M. Diffuse Intrinsic Pontine Glioma: New Pathophysiological Insights and Emerging Therapeutic Targets. *Curr Neuropharmacol*. 2017;15:88–97.
- Chiarelli PA, Chu JK, Krieger MD. Brainstem Tumors. In: Di Rocco C, Pang D, Rutka JT (eds). *Textbook of Pediatric Neurosurgery*. Springer International Publishing: Cham, 2019, pp 1–35.
- Warren KE. Diffuse intrinsic pontine glioma: poised for progress. *Front Oncol*. 2012;2:205.
- Kebudi R, Cakir FB. Management of diffuse pontine gliomas in children: recent developments. *Paediatr Drugs*. 2013;15:351–62.
- Van Gool SW, Makalowski J, Bonner ER, Feyen O, Domogalla MP, Prix L et al. Addition of multimodal immunotherapy to combination treatment strategies for children with DIPG: A single institution experience. *Medicines* 2020; 7.
- Koschmann C, Al-Holou WN, Alonso MM, Anastas J, Bandopadhyay P, Barron T, et al. A road map for the treatment of pediatric diffuse midline glioma. *Cancer Cell*. 2024;42:1–5.
- Garcia-Fabiani MB, Comba A, Kadiyala P, Haase S, Núñez FJ, Altshuler D, et al. Isolation and characterization of immune cells from the tumor microenvironment of genetically engineered pediatric high-grade glioma models using the sleeping beauty transposon system. *Methods Enzymol*. 2020;632:369–88.
- Hambardzumyan D, Amankulor NM, Helmy KY, Becher OJ, Holland EC. Modeling Adult Gliomas Using RCAS/t-va Technology. *Transl Oncol*. 2009;2:89–95.
- Larson JD, Kasper LH, Paugh BS, Jin H, Wu G, Kwon CH, et al. Histone H3.3 K27M Accelerates Spontaneous Brainstem Glioma and Drives Restricted Changes in Bivalent Gene Expression. *Cancer Cell*. 2019;35:140–155.e147.
- Katagi H, Louis N, Unruh D, Sasaki T, He X, Zhang A, et al. Radiosensitization by Histone H3 Demethylase Inhibition in Diffuse Intrinsic Pontine Glioma. *Clinical Cancer Res*. 2019;15:5572–83.
- Martinez-Velez N, Garcia-Moure M, Marigil M, Gonzalez-Huarriz M, Puigdelloses M, Gallego Perez-Larraya J, et al. The oncolytic virus Delta-24-RGD elicits an antitumor effect in pediatric glioma and DIPG mouse models. *Nature Commun*. 2019;10:2235.
- Mount CW, Majzner RG, Sundaresh S, Arnold EP, Kadapakkam M, Haile S, et al. Potent antitumor efficacy of anti-GD2 CAR T cells in H3-K27M(+) diffuse midline gliomas. *Nature Med*. 2018;24:572–9.
- Tsvankin V, Hashizume R, Katagi H, Herndon JE, Lascola C, Venkatraman TN et al. ABC Transporter inhibition plus dexamethasone enhances the efficacy of convection enhanced delivery in H3.3K27M mutant diffuse intrinsic pontine glioma. *Neurosurgery* 2019.
- Meel MH, Sewing ACP, Waranecki P, Metselaar DS, Wedekind LE, Koster J, et al. Culture methods of diffuse intrinsic pontine glioma cells determine response to targeted therapies. *Exp cell Res*. 2017;360:397–403.
- Andrade AF, Annett A, Karimi E, Topouza DG, Rezanejad M, Liu Y, et al. Immune landscape of oncohistone-mutant gliomas reveals diverse myeloid populations and tumor-promoting function. *Nature Commun*. 2024;15:7769.
- Liu I, Jiang L, Samuelsson ER, Marco Salas S, Beck A, Hack OA, et al. The landscape of tumor cell states and spatial organization in H3-K27M mutant diffuse midline glioma across age and location. *Nat Genet*. 2022;54:1881–94.
- Ross JL, Puigdelloses-Vallcorba M, Piñero G, Soni N, Thomason W, DeSisto J, et al. Microglia and monocyte-derived macrophages drive progression of pediatric high-grade gliomas and are transcriptionally shaped by histone mutations. *Immunity*. 2024;57:2669–2687.e2666.
- Grasso CS, Tang Y, Truffaux N, Berlow NE, Liu L, Debily MA, et al. Functionally defined therapeutic targets in diffuse intrinsic pontine glioma. *Nature Med*. 2015;21:555–9.
- Keshelava N, Seeger RC, Groshen S, Reynolds CP. Drug resistance patterns of human neuroblastoma cell lines derived from patients at different phases of therapy. *Cancer Res*. 1998;58:5396–405.

34. Kroesen M, Brok IC, Reijnen D, van Hout-Kuijter MA, Zeelenberg IS, Den Brok MH, et al. Intra-adrenal murine TH-MYCIN neuroblastoma tumors grow more aggressive and exhibit a distinct tumor microenvironment relative to their subcutaneous equivalents. *Cancer Immunol Immunother*. 2015;64:563–72.
35. Lin GL, Monje M. A protocol for rapid post-mortem cell culture of diffuse intrinsic pontine glioma (DIPG). *J Vis Exp*. 2017;121:55360.
36. Graw S, Tang J, Zafar MK, Byrd AK, Bolden C, Peterson EC, et al. proteiNorm - A User-Friendly Tool for Normalization and Analysis of TMT and Label-Free Protein Quantification. *ACS Omega*. 2020;5:25625–33.
37. Ritchie ME, Phipson B, Wu D, Hu Y, Law CW, Shi W, et al. limma powers differential expression analyses for RNA-sequencing and microarray studies. *Nucleic Acids Res*. 2015;43:e47.
38. Dobin A, Davis CA, Schlesinger F, Drenkow J, Zaleski C, Jha S, et al. STAR: ultrafast universal RNA-seq aligner. *Bioinformatics*. 2013;29:15–21.
39. Robinson MD, McCarthy DJ, Smyth GK. edgeR: a Bioconductor package for differential expression analysis of digital gene expression data. *Bioinformatics*. 2010;26:139–40.
40. Robinson MD, Oshlack A. A scaling normalization method for differential expression analysis of RNA-seq data. *Genome Biol*. 2010;11:R25.
41. You Y, Dong X, Wee YK, Maxwell MJ, Alhamdoosh M, Smyth GK, et al. Modeling group heteroscedasticity in single-cell RNA-seq pseudo-bulk data. *Genome Biol*. 2023;24:107.
42. De Vries A, Ripley BD, de Vries MA. Package 'ggdendro'2022.
43. Warnes MGR, Bolker B, Bonebakker L, Gentleman R, Huber W. Package 'gplots'. Various R programming tools for plotting data 2016.
44. Falcon S, Gentleman R. Using GOstats to test gene lists for GO term association. *Bioinformatics*. 2007;23:257–8.
45. Szklarczyk D, Gable AL, Nastou KC, Lyon D, Kirsch R, Pyysalo S, et al. The STRING database in 2021: customizable protein-protein networks, and functional characterization of user-uploaded gene/measurement sets. *Nucleic Acids Res*. 2021;49:D605–D612.
46. Shannon P, Markiel A, Ozier O, Baliga NS, Wang JT, Ramage D, et al. Cytoscape: a software environment for integrated models of biomolecular interaction networks. *Genome Res*. 2003;13:2498–504.
47. Ostermann S, Csajka C, Buclin T, Leyvraz S, Lejeune F, Decosterd LA, et al. Plasma and cerebrospinal fluid population pharmacokinetics of temozolomide in malignant glioma patients. *Clinical Cancer Res*. 2004;10:3728–36.
48. Bailey S, Howman A, Wheatley K, Wherton D, Boota N, Pizer B, et al. Diffuse intrinsic pontine glioma treated with prolonged temozolomide and radiotherapy: results of a United Kingdom phase II trial (CNS 2007 04). *Eur J Cancer*. 2013;49:3856–62.
49. He C, Xu K, Zhu X, Dunphy PS, Gudenas B, Lin W, et al. Patient-derived models recapitulate heterogeneity of molecular signatures and drug response in pediatric high-grade glioma. *Nature Commun*. 2021;12:4089.
50. Cui B, Johnson SP, Bullock N, Ali-Osman F, Bigner DD, Friedman HS. Decoupling of DNA damage response signaling from DNA damages underlies temozolomide resistance in glioblastoma cells. *J Biomed Res*. 2010;24:424–35.
51. Homan MJ, Franson A, Ravi K, Roberts H, Pai MP, Liu C, et al. Panobinostat penetrates the blood-brain barrier and achieves effective brain concentrations in a murine model. *Cancer Chemother Pharm*. 2021;88:555–62.
52. Vitanza NA, Biery MC, Myers C, Ferguson E, Zheng Y, Girard EJ, et al. Optimal therapeutic targeting by HDAC inhibition in biopsy-derived treatment-naïve diffuse midline glioma models. *Neuro-Oncol*. 2021;23:376–86.
53. Lin GL, Wilson KM, Ceribelli M, Stanton BZ, Woo PJ, Kreimer S, et al. Therapeutic strategies for diffuse midline glioma from high-throughput combination drug screening. *Sci Transl Med*. 2019;11:519.
54. Dalle Ore C, Coleman C, Gupta N, Mueller S. Advances and clinical trials update in the treatment of diffuse intrinsic pontine gliomas. *Pediatric Neurosurg*. 2023;58:259–66.
55. Baumann Z, Auf der Maur P, Bentires-Alj M. Feed-forward loops between metastatic cancer cells and their microenvironment-the stage of escalation. *EMBO Mol Med*. 2022;14:e14283.
56. Jayaram MA, Phillips JJ. Role of the microenvironment in glioma pathogenesis. *Annu Rev Pathol*. 2024;19:181–201.
57. Hashizume R, Ozawa T, Dinca EF, Banerjee A, Prados MD, James CD, et al. A human brainstem glioma xenograft model enabled for bioluminescence imaging. *J Neuro-Oncol*. 2010;96:151–9.
58. Monje M, Mitra SS, Freret ME, Ravesh TB, Kim J, Masek M, et al. Hedgehog-responsive candidate cell of origin for diffuse intrinsic pontine glioma. *Proc Natl Acad Sci USA*. 2011;108:4453–8.
59. Puech C, Hodin S, Forest V, He Z, Mismetti P, Delavenne X, et al. Assessment of HBEC-5i endothelial cell line cultivated in astrocyte conditioned medium as a human blood-brain barrier model for ABC drug transport studies. *Int J Pharm*. 2018;551:281–9.
60. Dello Russo C, Cappoli N, Coletta I, Mezzogori D, Paciello F, Pozzoli G, et al. The human microglial HMC3 cell line: where do we stand? A systematic literature review. *J Neuroinf*. 2018;15:259.
61. Sethi P, Jyoti A, Swindell EP, Chan R, Langner UW, Feddock JM, et al. 3D tumor tissue analogs and their orthotopic implants for understanding tumor-targeting of microenvironment-responsive nanosized chemotherapy and radiation. *Nanomedicine*. 2015;11:2013–23.
62. Upreti M. Tumor tissue analogs for the assessment of radioresistance in cancer stem cells. *Methods Mol Biol*. 2018;1692:117–28.
63. Ausejo-Mauleon I, Labiano S, de la Nava D, Laspeidea V, Zalacain M, Marrodán L, et al. TIM-3 blockade in diffuse intrinsic pontine glioma models promotes tumor regression and antitumor immune memory. *Cancer Cell*. 2023;41:1911–1926.e1918.
64. Kordowski A, Mulay O, Tan X, Vo T, Baumgartner U, Maybury MK, et al. Spatial analysis of a complete DIPG-infiltrated brainstem reveals novel ligand-receptor mediators of tumour-to-TME crosstalk. *Acta Neuropathol Commun*. 2025;13:35.
65. El-Khouly FE, Veldhuijzen van Zanten SEM, Santa-Maria Lopez V, Hendrikse NH, Kaspers GJL, Loizos G, et al. Diagnostics and treatment of diffuse intrinsic pontine glioma: where do we stand?. *J Neuro-Oncol*. 2019;145:177–84.
66. Duchatel RJ, Mannan A, Woldu AS, Hawtrey T, Hindley PA, Douglas AM, et al. Preclinical and clinical evaluation of German-sourced ONC201 for the treatment of H3K27M-mutant diffuse intrinsic pontine glioma. *Neuro-Oncol Adv*. 2021;3:vdab169.
67. Nagaraja S, Vitanza NA, Woo PJ, Taylor KR, Liu F, Zhang L, et al. Transcriptional dependencies in diffuse intrinsic pontine glioma. *Cancer Cell*. 2017;31:635–652.e636.
68. Hart MG, Garside R, Rogers G, Stein K, Grant R. Temozolomide for high grade glioma. *Cochrane Database Syst Rev*. 2013;2013:CD007415.
69. Rizzo D, Scalzone M, Ruggiero A, Maurizi P, Attinà G, Mastrangelo S, et al. Temozolomide in the treatment of newly diagnosed diffuse brainstem glioma in children: a broken promise?. *J Chemother*. 2015;27:106–10.
70. Vallero SG, Bertin D, Basso ME, Pittana LS, Mussano A, Fagioli F. Diffuse intrinsic pontine glioma in children and adolescents: a single-center experience. *Child's Nerv Syst ChNS*. 2014;30:1061–6.
71. Abe H, Natsumeda M, Okada M, Watanabe J, Tsukamoto Y, Kanemaru Y, et al. MGMT Expression Contributes to Temozolomide Resistance in H3K27M-Mutant Diffuse Midline Gliomas. *Frontiers Oncol*. 2019;9:1568.
72. Harttrampf AC, da Costa MEM, Renoult A, Daudigeos-Dubus E, Geoerger B. Histone deacetylase inhibitor panobinostat induces antitumor activity in epithelioid sarcoma and rhabdoid tumor by growth factor receptor modulation. *BMC Cancer*. 2021;21:833.
73. Laporte AN, Barrott JJ, Yao RJ, Poulin NM, Brodin BA, Jones KB, et al. HDAC and proteasome inhibitors synergize to activate pro-apoptotic factors in synovial sarcoma. *PLoS One*. 2017;12:e0169407.
74. Bota DA, Mason W, Kesari S, Magge R, Winograd B, Elias I, et al. Marizomib alone or in combination with bevacizumab in patients with recurrent glioblastoma: Phase I/II clinical trial data. *Neuro-Oncol Adv*. 2021;3:vdab142.
75. Lee EQ, Reardon DA, Schiff D, Drappatz J, Muzikansky A, Grimm SA, et al. Phase II study of panobinostat in combination with bevacizumab for recurrent glioblastoma and anaplastic glioma. *Neuro-Oncol*. 2015;17:862–7.
76. Cupit-Link M, Federico SM. Treatment of high-risk neuroblastoma with dinutuximab and chemotherapy administered in all cycles of induction. *Cancers*. 2023;15:4609.
77. Goldberg JL, Sondel PM. Enhancing Cancer Immunotherapy Via Activation of Innate Immunity. *Semin Oncol*. 2015;42:562–72.
78. Xiang M, Kim H, Ho VT, Walker SR, Bar-Natan M, Anahtar M, et al. Gene expression-based discovery of atovaquone as a STAT3 inhibitor and anticancer agent. *Blood*. 2016;128:1845–53.
79. Barbieri F, Verduci I, Carlini V, Zona G, Pagano A, Mazzanti M, et al. Repurposed biguanide drugs in glioblastoma exert antiproliferative effects via the inhibition of intracellular chloride channel 1 Activity. *Frontiers Oncol*. 2019;9:135.
80. Zou S, Tong Q, Liu B, Huang W, Tian Y, Fu X. Targeting STAT3 in Cancer Immunotherapy. *Mol Cancer*. 2020;19:145.
81. Zetterberg FR, MacKinnon A, Brimert T, Gravelle L, Johnsson RE, Kahl-Knutson B, et al. Discovery and Optimization of the First Highly Effective and Orally Available Galectin-3 Inhibitors for Treatment of Fibrotic Disease. *J Med Chem*. 2022;65:12626–38.
82. de la Nava D, Ausejo-Mauleon I, Laspeidea V, Gonzalez-Huarriz M, Lacalle A, Casares N, et al. The oncolytic adenovirus Delta-24-RGD in combination with ONC201 induces a potent antitumor response in pediatric high-grade and diffuse midline glioma models. *Neuro-oncology*. 2024;5:1509–25.
83. Wang C, Sinha S, Jiang X, Fitch S, Wilson C, Caretti V, et al. A comparative study of brain tumor cells from different age and anatomical locations using 3D biomimetic hydrogels. *Acta Biomater*. 2020;116:201–8.

84. Khamis ZI, Sarker DB, Xue Y, Al-Akkary N, James VD, Zeng C et al. Modeling human brain tumors and the microenvironment using induced pluripotent stem cells. *Cancers* 2023;15:1253.

## ACKNOWLEDGEMENTS

We thank Dr Michelle Monje for providing patient-derived DIPG cell lines established and verified in her laboratory. We gratefully acknowledge research support from Department of Defense office of the CDMRP RA210290 (MU), NIH National Institute of Neurological Disorders & Stroke K08NS125175-01A1 (PC), Wright Foundation, Keck School of Medicine, University of Southern California (PC), Otis Booth Foundation, CHLA (PC), Children's Cancer Research Fund (PC & MU), Alternatives in Research & Development Foundation (MU & PC), and National Institute of Health R25 CA225513 (AE). We acknowledge support from The Saban Research Institute (TSRI), CHLA for the Core Pilot Program for the use of Cellular Imaging Core (MU) and The National Resource for Quantitative Proteomics supported by NIH grant R24GM137786 for the pilot voucher for mass spectrometry-based proteomics (MU). This work was also supported by the Flow Cytometry Core TSRI, CHLA, as well as generous philanthropy from Andrew & Gislaine Schwartz, Harmon & Elaine Schwartz, and the CHLA community.

## AUTHOR CONTRIBUTIONS

MU and PC jointly conceived the study, designed the DIPG model and associated experiments and prepared the manuscript. MU collected the 3D cell culture and imaging data with contribution from AP, MT, AH, GEF, DSK, DT, JKA, TP, JH, and MU analyzed and interpreted the multi-omic data; SDB, SGM and AJT contributed to the collection, analysis, and interpretation of the Proteomic data; MZ, MSJ, AE-E, SD, MDK, ASM, BHG, SA, RAM and TCC provided conceptual advice and edited the manuscript. All authors discussed the results and implications and commented on the manuscript at all stages.

## COMPETING INTERESTS

(a) The authors declare that they have no known competing financial interests or personal relationships that could have appeared to influence the work reported in this paper. (b) All research activities undertaken were conducted in accordance with strict ethical principles and in compliance with regulations and policies that were reviewed and duly approved by the CHLA Regulatory Oversight

Committees, Institutional Biosafety Committee (IBC-20-003 and IBC-24-008) and Institutional Review Board (CHLA-21-00319). (c) Informed consent was obtained from all participants for collecting the blood samples and processed in accordance with an institutional review board approved protocol.

## ADDITIONAL INFORMATION

**Supplementary information** The online version contains supplementary material available at <https://doi.org/10.1038/s41388-025-03533-7>.

**Correspondence** and requests for materials should be addressed to Meenakshi Upreti or Peter A. Chiarelli.

**Reprints and permission information** is available at <http://www.nature.com/reprints>

**Publisher's note** Springer Nature remains neutral with regard to jurisdictional claims in published maps and institutional affiliations.



**Open Access** This article is licensed under a Creative Commons Attribution-NonCommercial-NoDerivatives 4.0 International License, which permits any non-commercial use, sharing, distribution and reproduction in any medium or format, as long as you give appropriate credit to the original author(s) and the source, provide a link to the Creative Commons licence, and indicate if you modified the licensed material. You do not have permission under this licence to share adapted material derived from this article or parts of it. The images or other third party material in this article are included in the article's Creative Commons licence, unless indicated otherwise in a credit line to the material. If material is not included in the article's Creative Commons licence and your intended use is not permitted by statutory regulation or exceeds the permitted use, you will need to obtain permission directly from the copyright holder. To view a copy of this licence, visit <http://creativecommons.org/licenses/by-nc-nd/4.0/>.

© The Author(s) 2025

Meenakshi Upreti<sup>1,2,3</sup>✉, Astgik Petrosyan<sup>2,4</sup>, Matthew E. Thornton<sup>5</sup>, Anahit Hovsepian<sup>2</sup>, G. Esteban Fernandez<sup>2</sup>, David S. Koos<sup>2</sup>, Stephanie D. Byrum<sup>6,7</sup>, Samuel G. Mackintosh<sup>6</sup>, Jacob K. Al-Husseini<sup>1</sup>, Tania Porras<sup>8</sup>, Joseph Ha<sup>1</sup>, Alan J. Tackett<sup>6</sup>, Miqin Zhang<sup>9</sup>, Malkiat S. Johal<sup>10</sup>, Anat Erdreich-Epstein<sup>3,8</sup>, Susan Durham<sup>1,3</sup>, Mark D. Krieger<sup>1,3</sup>, Ashley S. Margol<sup>3,8</sup>, Brendan H. Grubbs<sup>5</sup>, Timothy C. Chambers<sup>6</sup>, Shahab Asgharzadeh<sup>3,8</sup>, Rex A. Moats<sup>2,3,11</sup> and Peter A. Chiarelli<sup>1,2,3,12</sup>✉

<sup>1</sup>Division of Neurosurgery, Children's Hospital Los Angeles, Los Angeles, CA, USA. <sup>2</sup>The Saban Research Institute, Children's Hospital Los Angeles, Los Angeles, CA, USA. <sup>3</sup>Keck School of Medicine of University of Southern California, Los Angeles, CA, USA. <sup>4</sup>GOFARR Laboratory for Organ Regenerative Research and Cell Therapeutics in Urology, Division of Urology, Children's Hospital Los Angeles, Los Angeles, CA, USA. <sup>5</sup>Department of Obstetrics & Gynecology, Keck School of Medicine, USC, Los Angeles, CA, USA. <sup>6</sup>Department of Biochemistry & Molecular Biology, University of Arkansas for Medical Sciences, Little Rock, AR, USA. <sup>7</sup>St. Jude Children's Research Hospital, Memphis, TN, USA. <sup>8</sup>Cancer & Blood Diseases Institute, Children's Hospital Los Angeles, Los Angeles, CA, USA. <sup>9</sup>Clinical Research Division, Fred Hutchinson Cancer Research Center, Seattle, WA, USA. <sup>10</sup>Department of Chemistry, Pomona College, Claremont, CA, USA. <sup>11</sup>Department of Radiology, Children's Hospital Los Angeles, Los Angeles, CA, USA. <sup>12</sup>Division of Neurosurgery, Phoenix Children's Hospital, Phoenix, AZ, USA. ✉email: [mupreti@chla.usc.edu](mailto:mupreti@chla.usc.edu); [pchiarelli@chla.usc.edu](mailto:pchiarelli@chla.usc.edu)